

Characterization of FBK NUV-HD-Cryo SiPMs near LHe temperature

Fengbo Gu*

*Department of Nuclear Physics, China Institute of Atomic Energy,
Sanqiang Rd. 1, Fangshan district, Beijing, China, 102413.*

Junhui Liao†

*Department of Nuclear Physics, China Institute of Atomic Energy,
Sanqiang Rd. 1, Fangshan district, Beijing, China, 102413.*

*Department of Physics, Brown University,
Hope St. 182, Providence, Rhode Island, USA, 02912.*

*Yalong River Hydropower Development Company,
Ltd., 288 Shuanglin Road, Chengdu 610051, China.*

*Jinping Deep Underground Frontier Science and Dark Matter
Key Laboratory of Sichuan Province, Liangshan 615000, China.*

Meiyunan Ma, Zhuo Liang, Zhaohua Peng, Jian Zheng, Jiangfeng Zhou, Guangpeng An

*Department of Nuclear Physics, China Institute of Atomic Energy,
Sanqiang Rd. 1, Fangshan district, Beijing, China*

Lifeng Zhang, Lei Zhang

*Department of Nuclear Synthesis Technology, China Institute of Atomic Energy,
Sanqiang Rd. 1, Fangshan district, Beijing, China*

Yuanning Gao

School of Physics, Peking University

Fabio Acerbi, Andrea Ficorella, Alberto Gola, Laura Parellada Monreal

Fondazione Bruno Kessler, via Sommarive, 18, Trento, 38123, Italy

(Dated: Tuesday 18th March, 2025)

Abstract

Five FBK “NUV-HD-Cryo” SiPMs have been characterized at 7 K and 10 K, with 405 nm and 530 nm LED light, respectively. The dark current rate (DCR) was measured to be ~ 1 Hz for the ~ 100 mm²-size SiPMs, or 0.01 Hz/mm², which is ~ 7 orders lower than the DCR at room temperature (RT). Given the tiny DCR at these cryogenic temperatures, we measured the SiPMs’ I-V curves with such a method: illuminated the SiPMs with weak light, which differs from the conventional measurements at RT. Then, we measured the photo-detection efficiency (PDE), after-pulse (AP), and cross-talk (CT) with a bias voltage ranging from 6 to 11 V overvoltage (OV). At the OV interval (6 to 11 V), the PDE was between 20% - 45%, and the AP and CT were both between $\sim 5\%$ and $\sim 20\%$. Suppose the bias is ≥ 10 V OV, the PDE would be $\geq 40\%$, and the AP and CT are $\sim 20\%$. Combining all of the measurements, we are confident that the SiPMs can be equipped as the photosensors on liquid helium detectors, including but not limited to the time projection chambers, which we have proposed in hunting for low-mass dark matter directly and beyond.

I. INTRODUCTION

Liquid helium (LHe) detectors have been proposed or employed to search for solar neutrinos [1–3], dark matter [4–10], and neutron electron dipole moment (nEDM) [11–14]. When a particle interaction takes place within LHe, it will emit scintillation peaked at 80 nm [15, 16]. Given that no commercial photosensor is capable of detecting vacuum ultraviolet (VUV) light directly, a wavelength shifter such as tetraphenyl butadiene (TPB) is often implemented to convert it to visible light. As a rule of thumb, a photosensor should be as close as possible to the liquid or gas to avoid unnecessary light loss. Consequently, one of the requirements for the photosensor equipped on an LHe detector is that it should be functional near LHe temperature, ~ 4.5 K [17]. Previous measurements have shown that photomultipliers (PMTs) and silicon photomultipliers (SiPMs) can work at 4.5 K or below [12, 18–20]. However, as far as we know, there is no complete characterization of a photosensor near 4.5 K. Although PMTs have been widely equipped on liquid argon and liquid xenon time

* FengboGu@outlook.com

† junhui_liao@brown.edu; junhui.private@gmail.com

projection chambers (TPCs) [21–25], they are not suitable for LHe TPCs because helium gas can permeate through the glass into the vacuum space of the photosensor. If that happens, an increase in dark current and degradation of the breakdown voltage is foreseen; as a result, the PMTs will deteriorate or even out of work since a discharge could happen inside the tube [26]. As such, SiPMs might be the only photosensor option for LHe TPCs.

In the manuscript, we present the characterization of Fondazione Brune Kessler (FBK) “NUV-HD-Cryo” SiPMs near LHe temperature, including an I-V curve, the dark count rate (DCR), photo-detection efficiency (PDE), and the after-pulse (AP) and cross-talk (CT) probabilities. The paper will be organized as follows. We first explain the testing setup in section II. The detailed tests of the I-V curve, DCR, PDE, AP, and CT at 10 K will be addressed in section III. After finishing the measurements at 10 K, we updated our detector, which made the SiPMs reach a simulation-consistent lower temperature of 7 K. We re-tested most of the parameters at 7 K again, as shown in section V. Our discussions and summaries are in section VI.

II. THE TESTING SETUP INTRODUCTION

ALETHEIA, standing for A Liquid hElium Time projection cHambEr In dARk matter, aims to hunt for low-mass dark matter (100’s MeV/c² to 10 GeV/c²) with liquid helium-filled TPCs. To fully exploit the detector’s potential, the equipped photosensors should have a PDE greater than 40% near LHe temperature [9]. In addition, the I-V curve, DCR, AP, and CT must be measured to know whether the FBK NUV-HD-Cryo SiPMs’ performance suits the ALETHEIA project (and other applications mentioned above).

A. The setup

As schematically shown in Fig. 1, the LED, the photodiode, and the SiPMs are all in a 10 K environment, while the preamplifier and data acquisition (DAQ) are at room temperature (RT). The 70 cm SMA cable going through the cryocooler’s walls connects the SiPMs in cryogenic conditions to the preamplifier on the warm side. All parts in cryogenic temperature have been verified earlier to ensure their capability of working at 4 K or below, and the parts were put in warm because they cannot work at LHe temperature.

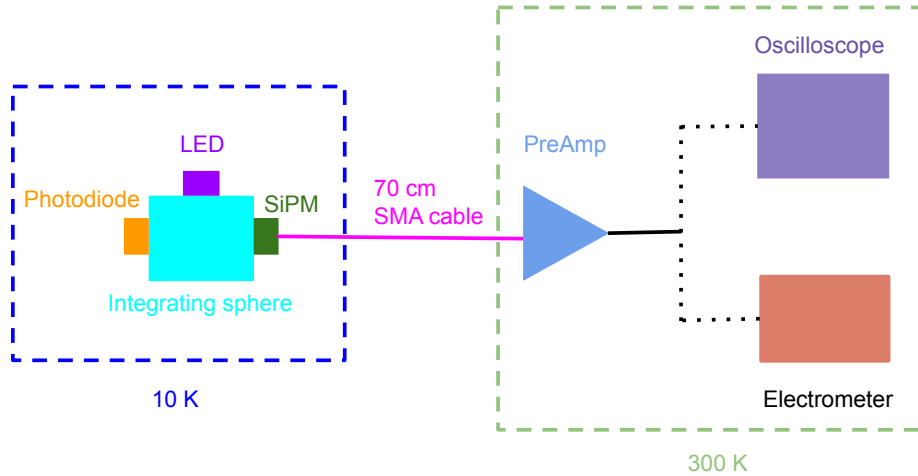


FIG. 1: The schematic drawing of the test setup. The LED, the photodiode, and the SiPMs are mounted on the integrating sphere’s surfaces, 90 degrees from each other. These parts are all at 10 K temperature. The 70 cm SMA cable conveys signals to the preamplifier at RT. Depending on the measurements, an 8 GHz bandwidth, 25 GSa/s sample rate oscilloscope, or a Keithley 6485 electrometer will be connected for data-taking.

Generally, a preamplifier should be located as close as possible to a detector to reduce signal deterioration on the cable. Reference [27] used a preamplifier capable of working at 40 K, so the amplifier was (only) a few cm away from the SiPMs in cryogenic. High electron mobility transistors (HEMTs) have been implemented as a preamplifier at 4 K and 10 mK [28, 29]. In contrast, some other references [20, 30] put the preamplifier at RT. In our setup, since the TI OPA694 chip integrated into the preamplifier cannot be functional at LHe temperature, we must leave the preamplifier at RT. The preamplifier circuit is based on the ultra wide-band, low-power, current feedback operational amplifier, OPA694, and is configured as a non-inverting voltage amplifier with a gain of 360. The amplifier is connected to the ground through a low-pass RC filter, composed of a $20\ \Omega$ serial resistor and a 1 nF capacitor, to reduce noise further. Depending on the data to take, an 8 GHz bandwidth, 25 GSa/s sample rate digital oscilloscope, or a Keithley 6485 electrometer will be utilized.

Fig. 2 shows the actual setup; the cubic integrating sphere mounts on the barely visible cooling plate, which is the cooling source of the detector system. The LED, the photodiode, the SiPMs, and the temperature sensor (TS) are all installed on the surfaces of the sphere.

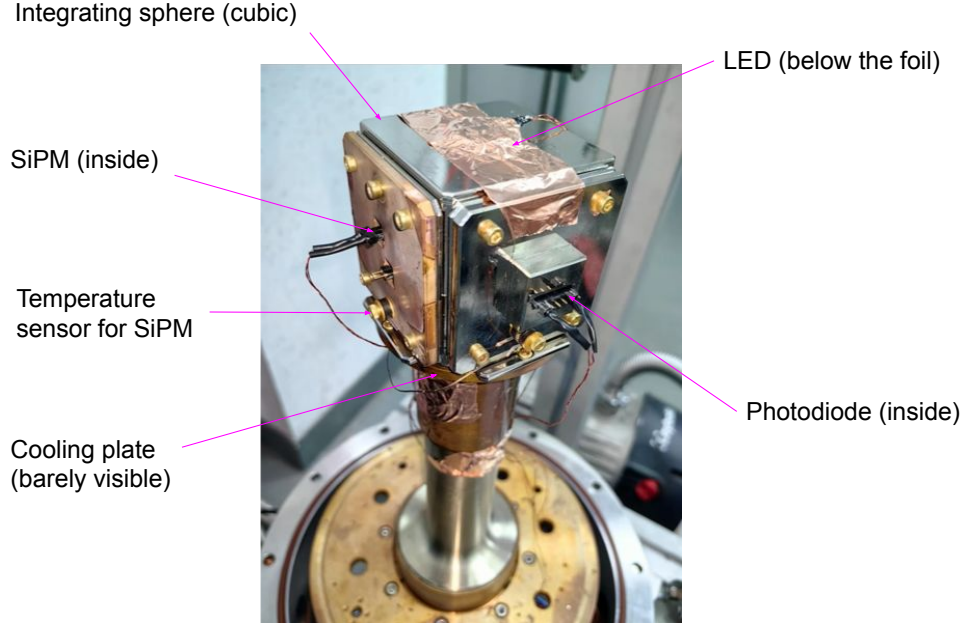


FIG. 2: The picture shows the integrating sphere mounted on the cooling plate (inside the G-M cryocooler). The photodiode, the LED, and the SiPMs are also visible in the image.

Being driven by the pulses produced in a signal generator, DG535 [31], the LEDs can emit monochromatic light with an intrinsic FWHM of $< 5\%$. The “NUV-HD-Cryo” SiPMs, having an active window of $11.7 \times 7.9 \text{ mm}^2$, a cell pitch of $30 \times 30 \mu\text{m}^2$, was thankfully provided by FBK company. We bought the $10 \times 10 \text{ mm}^2$ (active area) photodiode from Opto diode company [32]. For more info on the photodiode calibration, please refer to section II B.

Our team designed the integrating sphere and outsourced it to a commercial company in China. The inner surface of the 60 mm diameter integrating sphere is coated with highly reflective PTFE. The outside of the sphere is cubic, which gives convenience to (a) installing experimental parts on its surfaces and (b) being mounted securely on the cooling plate of the G-M cryocooler. As illustrated in Fig. 3, the LED, the calibrated photodiode, and the to-be-calibrated SiPMs are positioned 90 degrees from each other. This design ensures that the photodiode and the SiPMs receive the fixed ratio of photons as long as the size of the two corresponding ports does not change, regardless of the intensity profile of light emitted from the LED. In our case, the diameters of the ports for the photodiode and the SiPMs

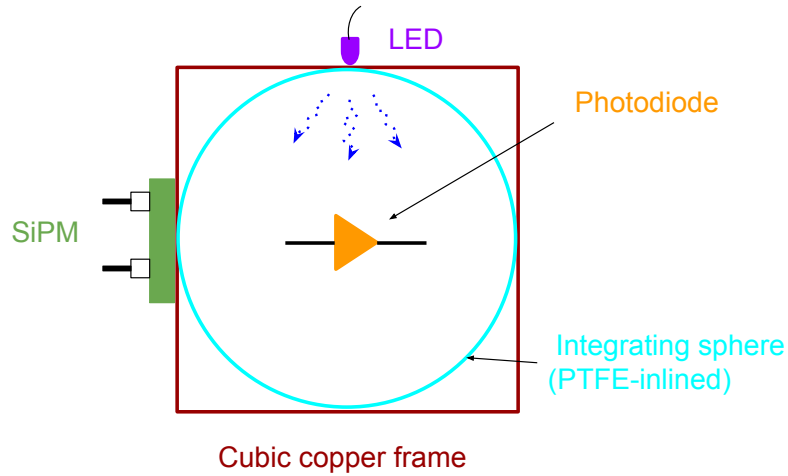


FIG. 3: The schematic drawing shows the PDE test setup. The inner surface of the integrating sphere is PTFE (not visible in the drawing). The LED simultaneously illuminates the to-be-calibrated SiPMs and the calibrated photodiode. Please refer to the main text for more information.

are 4.0 mm and 0.1 mm, respectively.

The cooling plate of the G-M cryocooler approaches its lowest temperature after ~ 3 hours of cooling; for the SiPMs on the integrating sphere, it will take a couple of additional hours to reach the lowest temperature. During our tests, we often run the cooling machine for more than 12 hours before launching a measurement to ensure the SiPMs and other parts on the sphere have reached the lowest temperature. Since it is impossible to measure the SiPMs' temperature accurately, in the paper, the SiPMs' temperature refers to the one measured on a TS ~ 5 cm away. According to our simulation, the SiPMs' actual temperature would be ~ 0.3 K higher than the sensor-measured value, as will be further discussed in section IV. We did not test the SiPMs at a temperature higher than 10 K because it is not the typical temperature the photosensor equipped on LHe detectors is likely to work; neither were the SiPMs characterized below 7 K due to the cryocooler's cooling power limitation.

B. Photodiode responsivity calibration at NIM in China

As mentioned in references [33–35], a to-be-tested SiPMs’ PDE can be figured out by measuring the relative efficiency between the SiPMs and a calibrated photodiode. That being said, the efficiency (responsivity) of the photodiode should be characterized in advance. The photodiode under test is AXUV100G from Opto diode company. Although the company’s website has a datasheet, we cannot implement the responsivity data directly for a calibration near 4.5 K since the official data sheet was measured at RT. Our original plan was to calibrate a couple of diodes at the National Institute of Standards and Technology (NIST). However, NIST cannot do the calibration near LHe temperature for the moment, though they would be capable of doing that in the future [36]. Luckily, a team at the National Institute of Metrology (NIM) in China agreed to calibrate our photodiodes in their G-M cryocooler as a side-project of their primary research programs. Although the NIM facility can only calibrate a photodiode with 405 and 530 nm light, the calibration is still valuable since the two wavelengths line up well with TPB-shifted LHe scintillation, $\sim 350 - 600$ nm [16].

We first asked the NIM team to calibrate the responsivity at RT to see whether their calibration is consistent with the official datasheet. As shown in Fig. 4, the red curve, representing the NIM calibrated results, overlaps well with the black curve, corresponding to the official datasheet. Then, two photodiodes were calibrated at 6 K, the lowest temperature the cryocooler can reach. The calibrated responsivity of the photodiode being implemented in the PDE tests as the two dots shown in Fig. 4.

During the calibrations at NIM, the temperature sensor and the photodiode were mounted on the same copper frame and separated ~ 8.0 cm. Our COMSOL simulation showed that the temperature difference between the photodiode and the temperature sensor was ~ 0.1 K, which is negligible compared to the temperature sensor’s 1.0 K uncertainty. Therefore, we consider the photodiode’s actual temperature during the calibration was directly measured by the sensor, 6 K.

III. CHARACTERIZING THE SIPMS AT 10 K

We characterized the SiPMs’ I-V curve, DCR, PDE, AP, and CT at 10 K in the winter of 2023. At that time, we thought 10 K was the lowest temperature the SiPMs could achieve

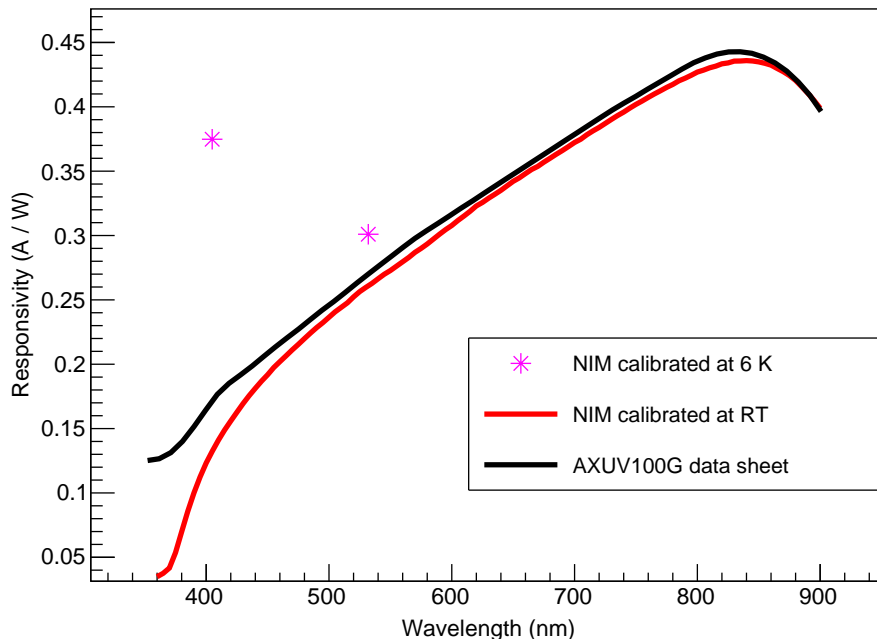


FIG. 4: The responsivity of the photodiode we used for PDE measurements. The black curve is copied from the photodiode’s datasheet. The red curve represents the data points measured at NIM at RT. The two stars were the photodiode’s characterized responsivity when they were cooled to 6 K and illuminated with 405 nm and 532 nm light, respectively.

until we launched a COMSOL simulation to understand the SiPMs’ accurate temperature. The simulation showed the SiPMs should be around 7 K instead of 10 K. It turned out that a tiny gap existed on the integrating sphere’s contacting surfaces, which induced cryogenics leakage. After filling the gaps with indium films, the SiPMs’ temperature reached 7 K, which was consistent with the simulation. We re-measured the parameters at 7 K again. For more info, please refer to section V.

A. Testing the SiPMs’ I-V curve at 10 K

We tested the FBK SiPMs’ I-V curve at ~ 4 K and RT in 2022 [9]. The I-V curves we measured at RT are consistent with the datasheet provided by FBK company at the same temperature. However, according to our communications with the company, they were unaware that any group has ever tested their SiPMs’ I-V curve near 4 K [37]. So, we were not sure whether our tests were correct or not in 2022, even though the shape of the I-V

curve seemed different from the one at RT: when the bias voltage is less than a threshold, the current is \sim nA; as long as the applied voltage reaches the criterion, the current jumps to \sim mA quickly, as the blue curve in Fig. 5 shows. Although we repeated the I-V curve tests several times by different personnel, the same results were observed. The puzzle was solved in 2023, when the dark current rate (DCR) of the SiPMs was measured. Since the DCR was as low as 1 Hz at 10 K, the dark current (mainly composed of single electron events) was too small to build up a μ A current, even if the bias was higher than the breakdown voltage [38]. As long as the bias voltage increases to a threshold much greater than 13 V overvoltage (OV), for example, the correlated noise increases significantly and eventually generates \sim mA current [37]. The 1 Hz DCR is equivalent to \sim 0.01 Hz/mm² for the \sim 100 mm² SiPMs, which is 7 orders lower than the same photosensor at RT, \sim 100 kHz/mm² [27].

Given the especially low DCR near LHe temperature, we tested the SiPMs' I-V curve in an alternative way: illuminating the SiPMs with weak pulsed light from an LED driven by a generator, DG535. During the DCR tests, the pulses used to drive the 405 nm LED were rectangular in shape, 4 V amplitude, 600 ns width, and 10 kHz frequency. Under such a testing setup, the I-V curve shows a conventional feature, as the green curve in Fig. 5. So far, we measured five randomly selected FBK SiPMs at 10 K with the same method, and all of the SiPMs recorded the same I-V curves. In addition, according to Fig. 5, the SiPMs' breakdown voltage at 10 K is around 26.0 V, which is consistent with other tests [24, 27], where 27.0 V and 32.0 V breakdown voltage were obtained on the similar SiPMs (NUV-HD-LF) at 40 K and RT, respectively. It is observed that the lower the temperature, the lower the breakdown voltage, possibly because a lower temperature would result in a higher electron ionization rate, as predicted in reference [39].

B. PDE measurements

The PDE of certain types of FBK SiPMs were measured at RT in references [24, 34]. A \geq 40% PDE was obtained with the bias voltage of 5 V overvoltage (OV) or higher. However, according to our communications with FBK company, their clients have yet to fully characterize the SiPMs' performance near LHe temperature [37]. Being inspired by the PDE calibrations on SiPMs performed at LAr or LXe temperatures [33, 34, 40–43], we characterized the PDE of the NUV-HD-Cryo FBK SiPMs near LHe temperature with 405

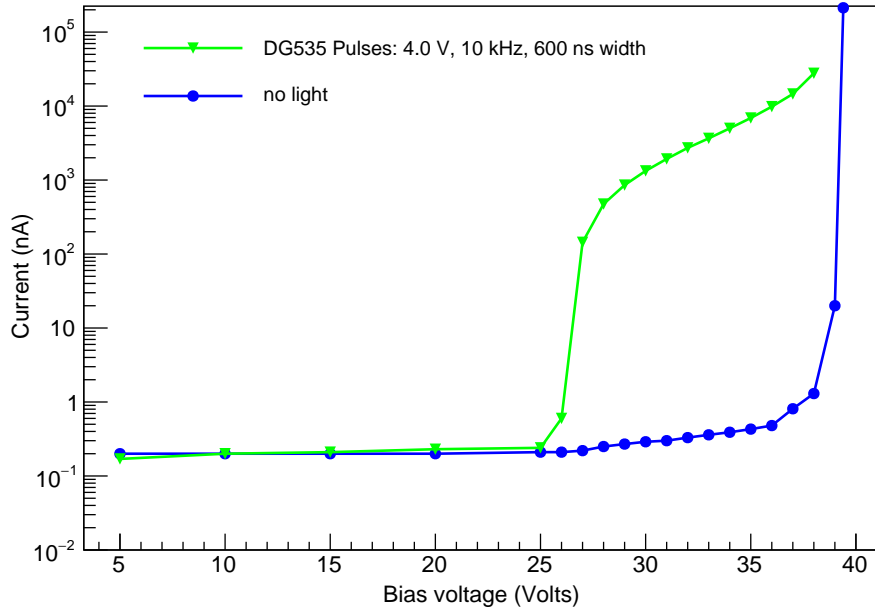


FIG. 5: The typical I-V curve of an FBK NUV-HD-Cryo SiPMs measured at ~ 10 K, with and without illumination. The green dots were measured with weak pulsed light from a 405 nm LED, which a DG535 drove. The blue ones were measured in the dark.

nm and 530 nm light.

1. PDE tests at 10 K

We implemented the photocurrent method to measure the PDE, as introduced in reference [34]. The PDE is calculated as Eq. (1),

$$PDE = \frac{\text{Measured_current}}{\text{Incident_current}} = \frac{I_{SiPM-L} - I_{SiPM-D}}{G \times q_e \times ECF \times Ph_I}, \quad (1)$$

where I_{SiPM-L} and I_{SiPM-D} are the measured current of the SiPMs with the light on and off, respectively; G is the gain of the SiPMs; q_e is the charge of an electron; ECF stands for Excess Charge Factor, which represents the fake efficiency prompt contributed from AP and CT [35, 44]; Ph_I is the incident photons.

Since a SiPMs' ECF is supposed to be the same with or without being illuminated, it can also be calculated when the SiPMs are in the dark,

$$ECF = \frac{I_{SiPM} - I_{Leak}}{G \times q_e \times N_D}, \quad (2)$$

where I_{SiPM} and I_{Leak} represent the measured current for the bias voltage above or below the breakdown voltage in the dark, respectively; the definition of G and q_e are the same as Eq. (1); N_D is the average number of photoelectrons per second in dark condition, which is equivalent to the average number of the Poisson statistical photoelectrons in a test [33, 34, 40–43]. As mentioned above in section III A, the SiPMs’ DCR is as low as 1 Hz near LHe temperature in the dark, which leads to ~ 0.1 pA current. While the measured current is ~ 0.1 nA, essentially the detector system’s dark current. So, we illuminated the SiPMs with a weak pulsed light for the ECF tests to have a μ A scale current. Effectively, our testing condition of “weak light at LHe temperature” is equivalent to the conventional one of “dark at RT”.

Substituting Eq. (2) into Eq. (1), one gets the PDE expression as Eq. (3).

$$PDE = \frac{N_D \times (I_{SiPM-L} - I_{SiPM-D})}{(I_{SiPM} - I_{Leak}) \times Ph_I}, \quad (3)$$

The SiPMs were illuminated with 405 nm or 503 nm light from an LED driven by a DG535 pulse generator. For PDE tests, the pulses from the DG535 are 4 V amplitude, 240 ns width, and 10 kHz frequency. Whenever the DG535 generated a pulse, it also triggered an 8 GHz bandwidth, 25 GSa/s sample rate oscilloscope to record the waveform showing on the screen. A typical single photoelectron (Phe) signal of the FBK SiPMs at 10 K is shown in Fig. 6. Given that (a) the effective time window of the pulses is 2.4×10^{-3} s ($= 240$ ns \times 10 kHz) per second, and (b) the DCR is about 1 Hz near LHe temperature, the dark current events only have a chance of 0.24% ($= 2.4 \times 10^{-3}$ s / 1 s) to show up in data. Therefore, the DCR will not smear the PDE results.

As mentioned above, we must figure out the average number of photoelectrons to calculate PDE. We get it through a fit on a charge histogram as shown in Fig. 7. The histogram was obtained by integrating thousands of analog signals in a ~ 10 μ s window. Fig. 6 shows such a typical signal. During data-taking, the DG535 was tuned to generate weak enough light to produce ~ 1.5 Phe in the SiPMs on average. The oscilloscope was triggered by the DG535. The signals were firstly recorded in the oscilloscope, then analyzed offline with ROOT [45]-based scripts. A recorded raw signal often contained roughly 2000 data points,

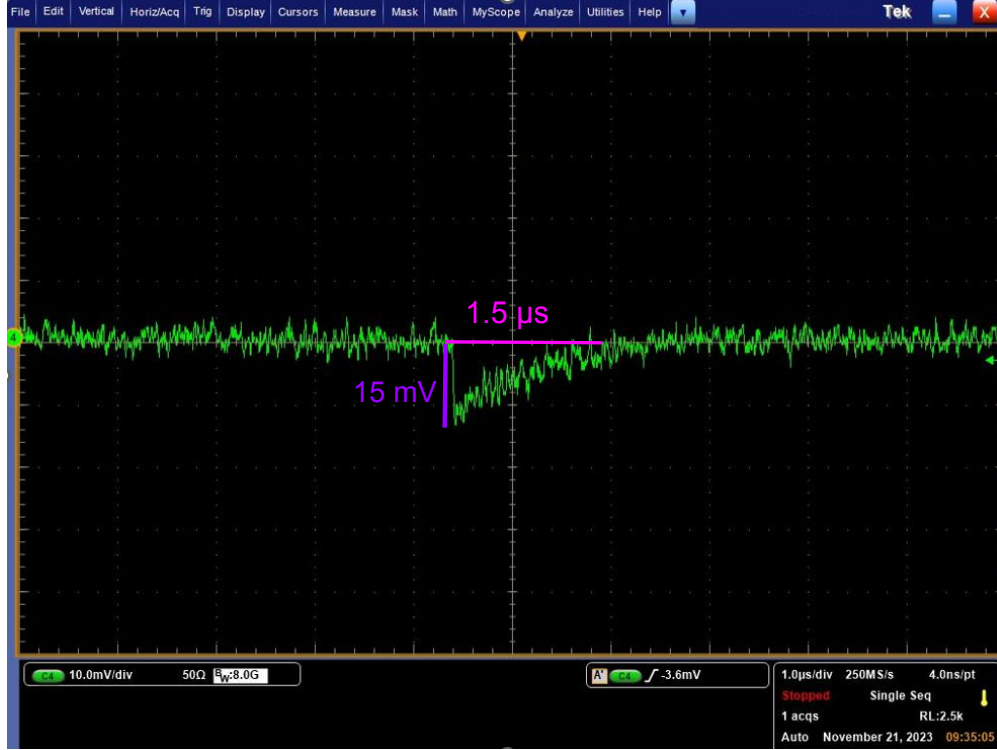


FIG. 6: A typical single Phe signal of the FBK SiPMs measured at 10 K.

which were integrated directly (without baseline subtraction), then divided by a 50 ohm (the input resistance of the oscilloscope) to convert into charge. Next, we multiplied the charge with an estimated gain to get the tentative number of Phe, as shown in Eq. (4),

$$\text{tentative } N_{\text{Phe}} = \frac{\text{raw signal integral}}{50\Omega \times (\text{estimated gain}) \times 1.6 \cdot 10^{-19}}, \quad (4)$$

where the *raw signal integral* is the integral of raw signals, 50Ω is the input resistance of the oscilloscope, the *estimated gain* is the estimated gain of the SiPMs (often is $1.0 \cdot 10^6$), $1.6 \cdot 10^{-19}$ is the charge of an electron. Fig. 7 shows a typical charge distribution and a fit. The fit function is Gaussian convoluted Poisson, as shown in Eq. (7).

$$\text{pedestal} = e^{-\mu} [\text{Gauss}((x - x_{\text{shift}}) \cdot x_{\text{scale}}, 0, p_{\text{width}})] \quad (5)$$

$$n\text{PhePeaks} = \sum_{n=1}^N \frac{e^{-\mu}}{n!} \mu^n [\text{Gauss}(x - x_{\text{shift}}) \cdot x_{\text{scale}}, n, \sqrt{n} \cdot \text{Gaus_width}] \quad (6)$$

$$\text{fitFunction} = Y_{\text{scale}} (\text{pedestal} + n\text{PhePeaks}) \quad (7)$$

The meaning of the parameters in the above equations are the following. “*pedestal*”,

“*nPhePeaks*”, and “*fitFunction*” are the fit functions correspond to the pedestal (or 0 Phe), 1 to N Phe peaks, and the whole histogram, respectively. “ μ ” is the average number of the Poisson function (“ μ ” is also equivalent to the “N_Phe” in Fig. 7 and the N_D in Eq. (3)). “*Y_scale*” means the scale factor of the fit function on the Y-axis. “*X_shift*” indicates the shift on the X-axis, which is the analog signals’ baseline shift on the oscilloscope. “*X_scale*” corresponds to the scale factor on the X-axis, which is the “correction” to the estimated gain in Eq. (4). “*Gaus_width*” and “*p_width*” are the $1\text{-}\sigma$ of the one Phe peak and the pedestal distribution, respectively.

In Fig. 7, the solid green curve represents the fit function, composed of several Poisson-weighted Gaussian functions, and the broken lines marked with “0 Phe”, “1 Phe” ..., and “4 Phe” are the mean values of these functions, as the dotted colorful curves show. However, the fit results in the statistics box do not correspond to the green curve; instead, they represent the fit function that has only been applied partly on the histogram ($\lesssim 2.0$ Phe), as the red-on-green part of the curve shows. We limited our fit function within the range to avoid smearing the fit by AP and CT events. The meaning of the parameters in the statistics box are the same as Eq. (5) and (6). The “*N_Phe*” is equivalent to the “ μ ” in the equations.

As mentioned above, since the gain in Eq. (4) was an estimated value; as a result, the X-axis in Fig. 7 does not represent the exact number of Phe; instead, it’s only a tentative one. With the fit results, the real number of Phe can be obtained with Eq. (8).

$$\text{real N_Phe} = (\text{tentative N_Phe} - \text{X_shift}) \cdot \text{X_scale}, \quad (8)$$

With the analysis shown in Eq. (8), the new histogram’s X-axis number would line up with the number of Phe, as we have done in our previous work [46]. However, we did not do the analysis in Fig. 7 because (a) it is not absolutely necessary to do that in some circumstances since as long as the N_Phe ($N \geq 1$) positions can be located on the histogram’s X-axis precisely, the photosensor’s response would be well understood [47, 48] and (b) the following CT analysis relies on Fig. 7. For more info on the charge histogram and the fit function, please refer to reference [46]. In the specific example, the average number of photoelectrons, 1.405 ± 0.304 Phe, is the N_D to be substituted in Eq. (3) for PDE calculation. Fig. 7 does not have separated Phe peaks as the similar SiPMs tested in references [24, 34]. We currently are not able to fully interpret the feature. This topic will be further discussed in

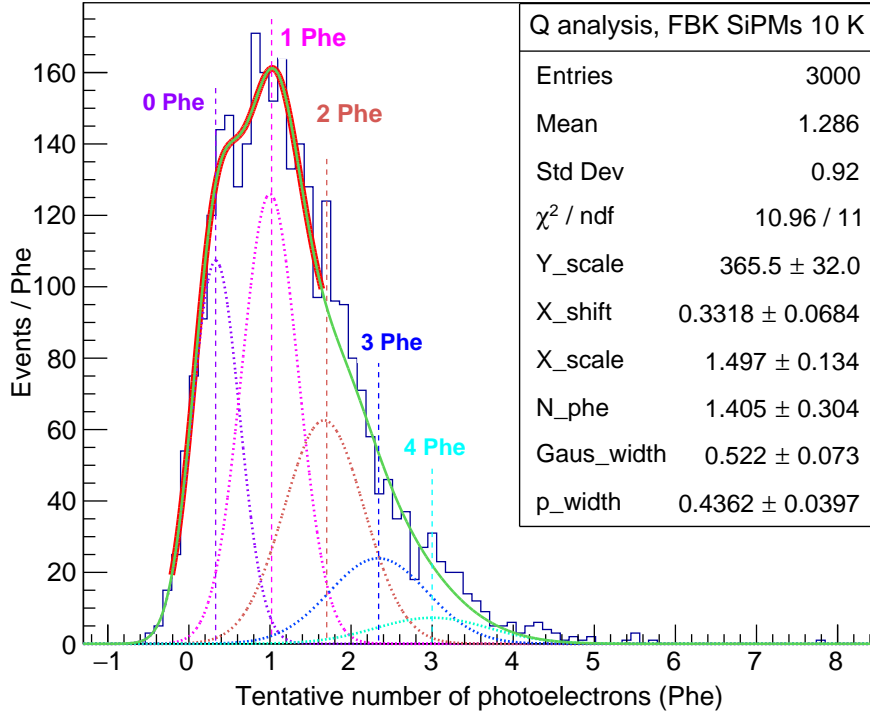


FIG. 7: A typical charge distribution we measured at 10 K for an FBK NUV-HD-Cryo SiPMs being biased with $OV = 9 \text{ V}$ (35 V). The fit function is Gaussian convoluted with Poisson [46]. For more info on the figure, please refer to the main text.

section VI A 1.

All of the parameters we measured or calculated for the PDE test are shown in table I. Submitting these parameters into Eq. (3) gives the PDE of $(39.50 \pm 8.77)\%$. Following the same procedure, the PDE values measured with other bias voltages and 530 nm light can also be obtained, as shown in Fig. 8. From the plot, we can see that for a bias voltage of 10 V OV or more, the PDE is equal to or greater than 40%.

As shown in Fig. 8, the uncertainties of the PDE under the two wavelengths are around $\sim 8\%$. According to our analysis, 95% of the uncertainty was from the average number of photoelectrons in charge fit, N_D . A feature of separated photoelectron peaks, such as the $6\times$ smaller ($4.0 \times 4.0 \text{ mm}^2$) FBK SiPMs measured in reference [24, 34], should be helpful to decrease N_D 's error bar and the PDE's uncertainty significantly.

TABLE I: All of parameters were used for a PDE calculation, in which the SiPMs were illuminated by 405 nm light, biased with 35 V (OV = 9 V) bias voltage, and operated at 10 K.

N_D (Phe)	I_{SiPM-L} (μA)	I_{SiPM-D} (nA)	I_{SiPM} (nA)	I_{Leak} (nA)	Ph_I (photon)	PDE (%)
1.41 ± 0.30	5.30 ± 0.09	0.12 ± 0.07	2.76 ± 0.02	0.02 ± 0.01	$(6.83 \pm 0.31)E6$	39.50 ± 8.77

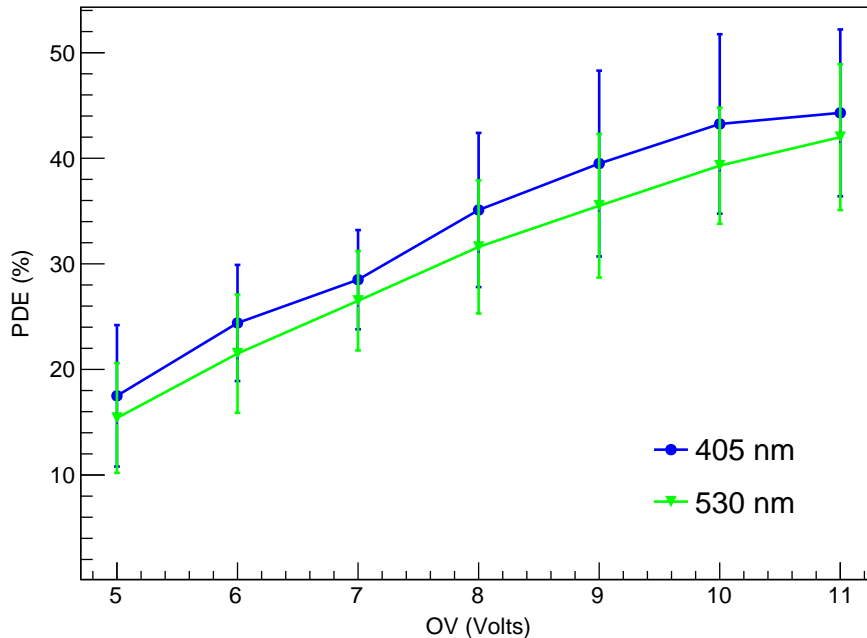


FIG. 8: The measured PDE for an FBK NUV-HD-Cryo SiPMs working at 10 K under variant bias voltages illuminated with 405 nm and 530 nm light. The PDE equals or exceeds 40% at ≥ 10 V OV.

2. PDE tests at RT

Although our SiPMs are supposed to work at LHe temperatures, we measured the PDE at RT with a similar setup and procedure at 10 K, as shown in Fig. 9. The PDE results are consistent with the measurements on the similar FBK SiPMs at RT [24, 34]. From Fig. 8 and 9, we can see (or extrapolate) that the PDE is significantly higher at RT than at 4 K under the same bias voltage. Specifically, for the bias of 5 V OV, the discrepancy between

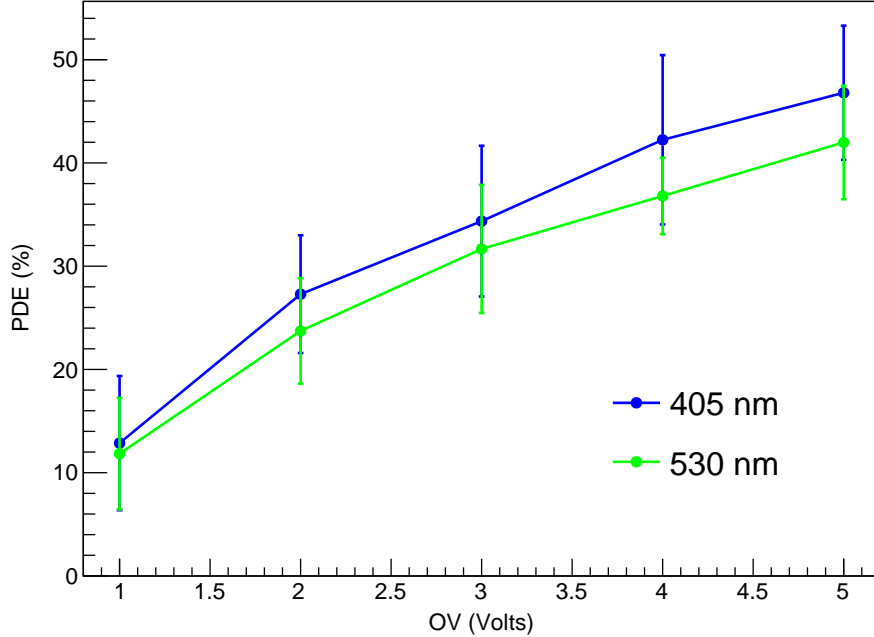


FIG. 9: The measured PDE for an FBK SiPMs working at RT under variant bias voltages illuminated by 405 nm and 530 nm light. The PDE values are consistent with the measurements on similar FBK SiPMs at RT [24, 34].

RT and 4 K for 405 nm and 530 nm light are 27% (45% - 18%) and 26% (42% - 16%), respectively. Though a thorough understanding of the feature of the lower the temperature, the lower the SiPMs PDE still lacks, our test results are consistent with references [49, 50].

3. Gain tests at 10 K

We tested the SiPMs' gain at 10 K with 405 nm light. The gain calculation was based on the charge histogram as Fig. 7. With the fit results and Eq. (8), a new histogram can be obtained in which the values on the X-axis would line up with the number of Phe (including the single photoelectron peak) and the real gain can be extrapolated, as we have done in our previous work [46]. As discussed above, with the fit results, X_{scale} , the gain can be "corrected". Fig. 10 shows the gain under variant OV voltages. With the same bias voltage of OV = 5 V, the gain of the NUV-HD-Cryo SiPMs at 10 K was 0.23×10^6 ; while the gain of the NUV-HD-LF type of SiPMs at 40 K was $\sim 0.32 \times 10^6$ [24, 27]. Given that the feature of the lower the temperature, the smaller the gain was observed in the two references, we

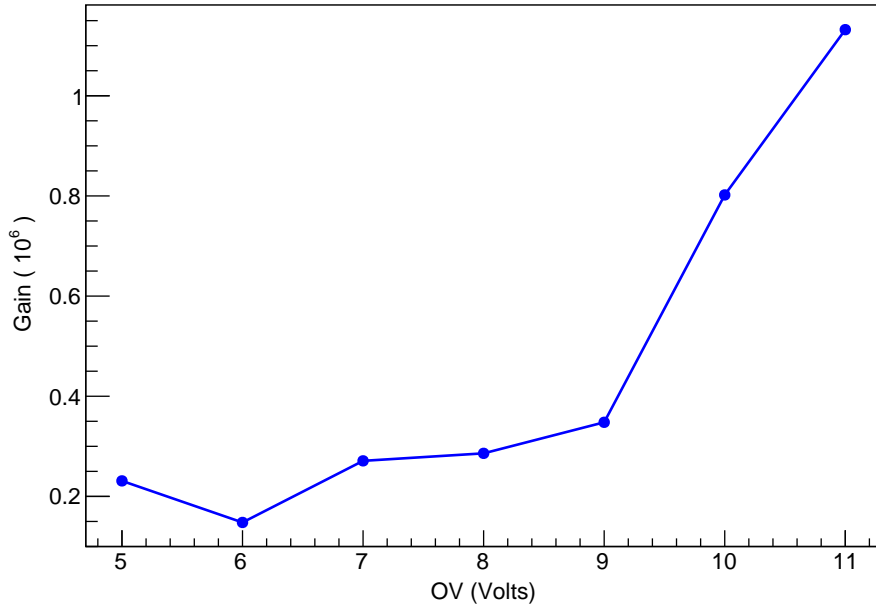


FIG. 10: The measured gain of an FBK SiPMs at 10 K, being illuminated by 405 nm light. For more info, please refer to the main text.

consider our results consistent with the previous measurements.

C. DCR, AP, and CT tests at 10 K

The dark current rate (DCR), after-pulse (AP), and cross-talk (CT) are critical parameters for SiPMs. Although these parameters were measured for two types of FBK SiPMs from RT down to 40 K, as shown in reference [27, 34], we must characterize them near LHe temperature again for the following reasons. (a) The SiPMs under our tests are not the same model as the references according to our discussion with FBK engineers [37], though it is similar to the NUV-HD-LF one. (b) The dimension of our SiPMs is $11.7 \times 7.9 \text{ mm}^2$, which is a factor of six greater than the ones tested in reference [27, 34], $4.0 \times 4.0 \text{ mm}^2$; the cell pitch of our SiPMs is $30 \times 30 \mu\text{m}^2$, which is also bigger than the $25 \times 25 \mu\text{m}^2$ one in the references. (c) For FBK SiPMs, the lowest temperature the DCR, AP, and CT have been tested was 40 K, while the working temperature of the SiPMs equipped on LHe detectors is supposed to be near LHe temperature; so, we need to test these parameters near $\sim 4.5 \text{ K}$.

1. DCR tests at 10 K

The setup for the DCR tests is nearly identical to the PDE tests, as shown in Fig. 2. However, the electronics are slightly different: a $5\times$ amplifier was connected to the preamplifier, and a counter read the signals coming out of the amplifier. Another difference was that the LED was off during the DCR tests. The counter was in a self-trigger model: once the signal's amplitude crosses the counter's threshold, the signal will be registered, and the count number will increase by one accordingly.

For the NUV-HD-Cryo type SiPMs under test, Fig. 11 shows the measured DCR is ~ 0.01 Hz/mm² for OV 10 V and 12 V at 10 K. Reference [27] measured the DCR for two types of FBK SiPMs: NUV-HD-SF and NUV-HD-LF. At RT, the typical DCR with 4 to 6 V OV is ~ 100 kHz, while at 40 K, the DCR is 0.1 Hz/mm² and 0.001 Hz/mm² for the NUV-HD-SF and NUV-HD-LF SiPMs, respectively. Given that (a) the dimension of our SiPMs is ~ 6 times that of the ones tested in the reference, and (b) the OV in our tests (10 to 12 V) is 6 volts higher than the paper (4 to 6 V), we consider our DCR results are consistent with the NUV-HD-LF ones measured in the paper at 40 K. We stick to a 10 V OV instead of a lower bias because it is the voltage the SiPMs can reach a required PDE criterion for LHe TPCs, 40%.

2. AP tests at 10 K

The setup for the AP tests is almost the same as the DCR measurements (the LED was off either); the only difference is that the counter was replaced with a digitizer, the DAQBOX-4-125 model, from TOFTEK company in China. The digitizer has a 125 MSPS sampling rate, a 12-bit resolution, and an input range of -1 V to +1 V. It operates in an auto-trigger mode: whenever a signal's amplitude crosses a programmable threshold, the timing crossing the threshold will be registered as the pulse's time, T_0 . A user-definable time interval will be used to define a time window. Assuming the interval is set to be 1 second, the time window would be $(T_0, T_0 + 1)$ s. And all of the pulses within the window will be registered. For each recorded pulse, the time is the difference between its threshold-crossing timing and the T_0 ; the charge is the integration of the analog signal (by the digitizer). Fig. 12 shows the time and charge info of the signals recorded in 10 seconds. During data-taking, the

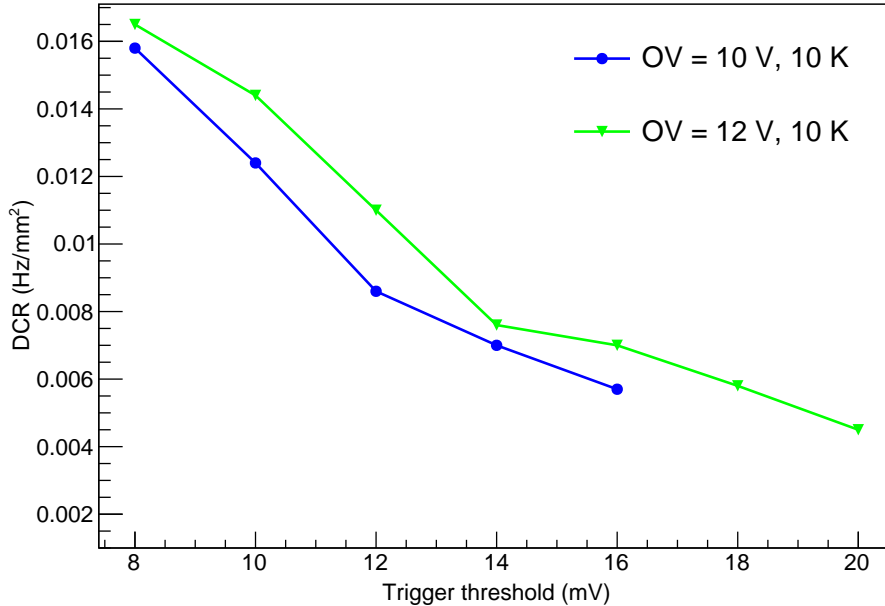


FIG. 11: The DCR of an FBK NUV-HD-Cryo type SiPMs at 10 K with the bias voltage of OV 10 V and 12 V. The SiPMs' dimension is $11.7 \times 7.9 \text{ mm}^2$ with the cell pitch of $30 \times 30 \text{ }\mu\text{m}^2$.

threshold was set to be 40 mV [51], and the time window of each pulse was $2 \text{ }\mu\text{s}$. The $2 \text{ }\mu\text{s}$ time window is wide enough for the $\sim 1.5 \text{ }\mu\text{s}$ width signals (Fig. 6) and narrow enough to exclude unnecessary noises. As shown in Fig. 12, there are 768 AP events and 4076 primary DCR and CT events. The AP ratio is calculated to be $768 / (768 + 4076) = 15.9\%$.

At 10 K, we also tested the AP under other bias voltages, as Fig. 13 shows. The measured AP rate at 10 K is (surprisingly) consistent with the results at 40 K [27] for the NUV-HD-LF type SiPMs in the sense that (a) the relationship between the bias voltage and the AP rate is the same: the higher the bias, the greater the AP; and (b) with the same bias voltage of OV 5 V or 6 V, the measured rate are both around $\sim 10\%$.

3. CT tests at 10 K

As shown in Fig. 12, the CT and primary DCR events overlap on the time-charge plane. These two categories of events can not be distinguished in timing because the CT events intrinsically have the exact timing as the primary DCR ones. On the other hand, since the

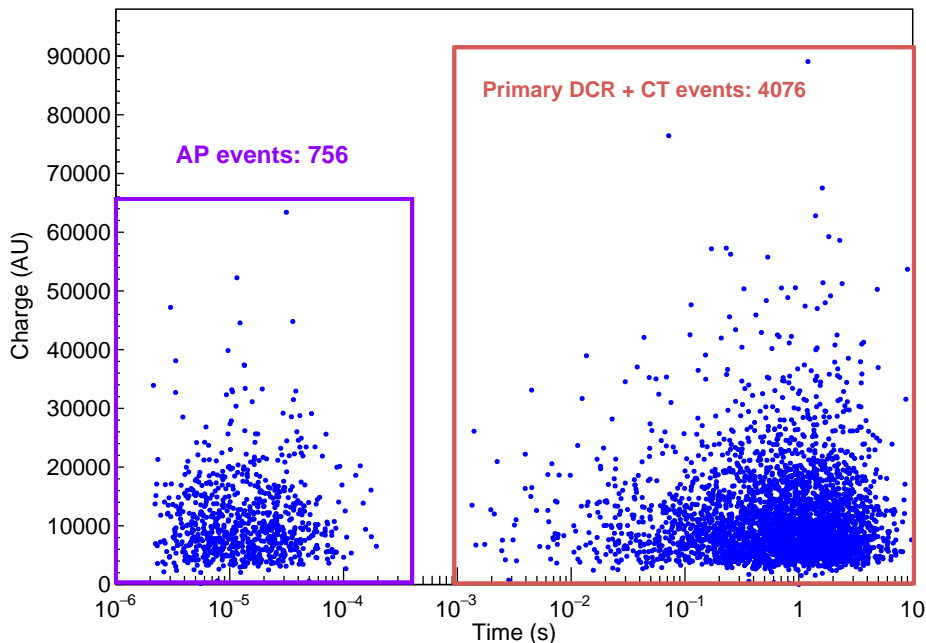


FIG. 12: The measured AP, primary DCR, and CT events for an FBK SiPMs biased with 9 V OV (i.e., 35 V) at 10 K.

charge distribution does not feature individual peaks, as Fig. 7 shows, we cannot do the CT analysis as reference [27]. By assuming (a) the CT photons propagated as a branching Poisson process and (b) the signals produced in the SiPMs followed the Borel distribution, reference [52] modeled the CT events well for the SiPMs operated at RT. In this work however, we figured the CT out for the SiPMs near LHe temperature in an alternative way, as follows.

The data for the CT analysis was the same as for the charge analysis when the SiPMs was illuminated with weak light, as shown in Fig. 7. The CT analysis can be split into three steps: (a) making a charge fit between the “0 Phe” and “1 Phe” region only, as the red-on-green part of the curve in Fig. 7 shows; (b) based on the fit results in step (a), extrapolating the actual number of events of the histogram, N_{actual} , under the (reasonable) assumption of no CT events included; (c) calculating the CT rate with the equation of $(N_{\text{all}} - N_{\text{actual}}) / N_{\text{all}}$, where N_{all} is the charge histogram’s total events, which is 3000 in Fig. 7. We believe almost all of the $(N_{\text{all}} - N_{\text{actual}})$ events are the CT events, while the AP ones are minimum because (i) although the oscilloscope screen has a window of 10 μs and the SiPMs’ signal is

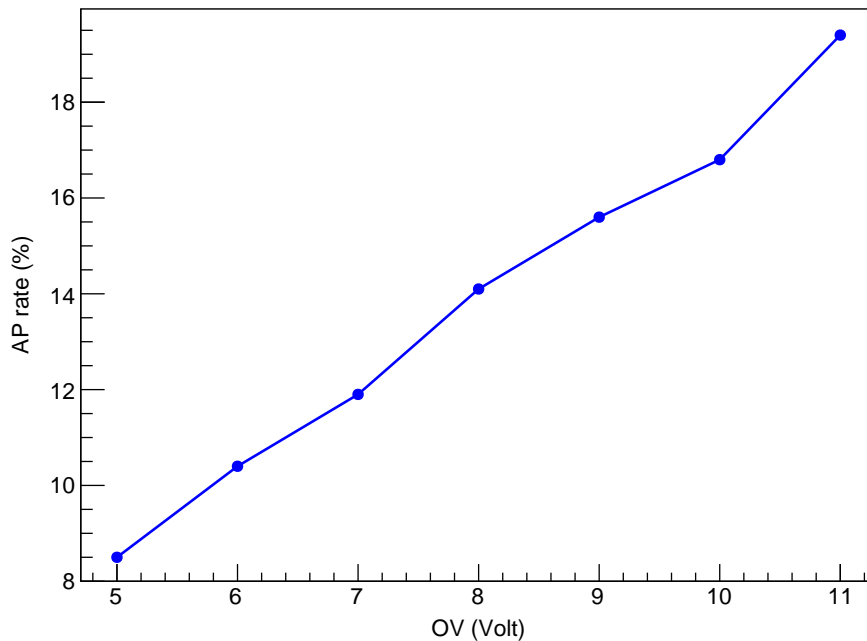


FIG. 13: The AP rate of the FBK SiPMs working at 10 K when biased with 9 V OV (35 V).

relatively narrow, $1.5 \mu\text{s}$, as shown in Fig. 6, we have set a $2 \mu\text{s}$ time window on the screen with cursors in data taking to make sure only the “true” signals (inside of the $2 \mu\text{s}$ window) have been analyzed, while the “fake” events (outside of the window) have been excluded; and (ii) as shown in Fig. 12, all of the AP events have a $\geq 2 \mu\text{s}$ delay from the primary DCR events. As a result, Fig. 7 would only have ignorable AP events, and $(N_{\text{all}} - N_{\text{actual}})$ represents CT events.

Since the charge fit has already been introduced in detail in section III B 1 above and step (c) is very straightforward, we mainly focus on step (b) here. We first select part of the histogram and the fit function, on which the equivalent relationship between the number of events of the partial histogram and the area of the partial fit function can be built. Then, we extrapolate the N_{actual} with the relationship and the area of the total fit function. In the following, we intentionally ignore the units to simplify the analysis.

Only one of the 388 selected events was contributed from the “2 Phe” events (The event would be visible as long as the Y-axis is on a log scale). The area of the partial fit function is the integration between -1 and 0.3318, 42.5221 ± 1.6260 , which corresponds to the region

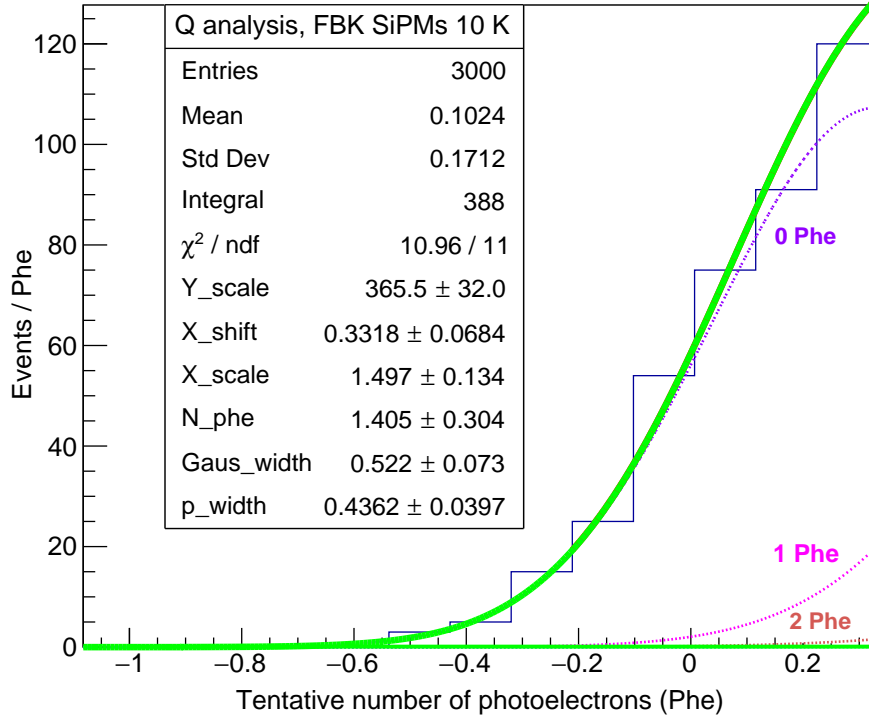


FIG. 14: The selected range, $Q < 0.3318$, of Fig. 7. The number of events for the selected histogram is 388, as the “Integral” value in the statistics box shows. The area of the region enclosed by the (green) fit function curve, the X-axis, and the $X = 0.3318$ line is 42.5221.

being enclosed by the fit curve, the X-axis, and the $X = 0.3318$ line in Fig .14. The integral of 42.5221 and its uncertainty of 1.6260 were obtained from calling the fit function’s ROOT-inlined functions, “Integral ()” and “IntegralError ()”, respectively. Given the quality of the fit in Fig. 7, the area of 42.5221 and the 388 events can be considered equivalent. Since the area of the whole fit function (X from -1 to 8 of Fig. 7) is 314.8500 ± 5.7451 , the histogram should have 2872.9014 ± 121.7230 “actual” events (without CT events interference), as Eq. (9) extrapolates,

$$\text{The extrapolated “actual” events} = 388 \times \frac{314.8500 \pm 5.7451}{42.5221 \pm 1.6260} = 2872.9014 \pm 121.7230, \quad (9)$$

As Fig. 7 indicates, the charge histogram has 3000 events in total, which means there are 127.0986 ± 121.7230 ($= 3000 - (2872.9014 \pm 121.7230)$) events contributed from CT. The CT event ratio can be calculated as Eq. (10),

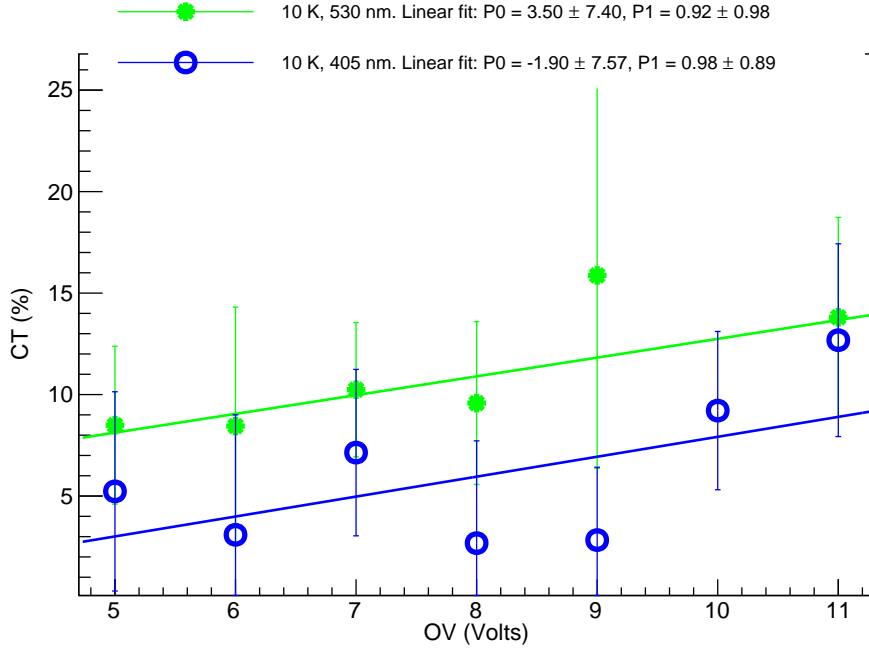


FIG. 15: The CT rate for the FBK SiPMs operating at 10 K, illuminated with 405 and 530 nm light and biased with an OV from 5 V to 11 V. The linear fit results on the CT rate data are shown on the top of the plot. P0 is the constant, and P1 is the slope. For more info on the analysis, please refer to the main text.

$$\text{CT event rate} = (127.0986 \pm 121.7230)/3000 = (4.23 \pm 4.06)\%, \quad (10)$$

which is similar to the measured CT for the NUV-HD-LF type of FBK SiPMs biased with OV = 3 V at 40 K, 6% [34]. Under higher bias voltages (OV = 4, 5, 6 V), the measured CT in the reference is between 10 and 16%. We measured the SiPMs' CT being biased with 5 to 11 V OV and calculated the uncertainties, as summarized in Fig. 15. In the plot, all of the CT rate values and their uncertainties were normalized to have 1.0 Phe. Further, a linear fit was applied to fit the CT rate data. P0 is the constant, and P1 is the slope. We saw the expected trend of the higher the bias, the greater the CT rate.

IV. UNDERSTANDING THE SiPMs' TEMPERATURE

In parallel to testing the SiPMs' performance at 10 K, we launched a COMSOL [53] simulation to crosscheck whether the 10 K temperature measured by the sensor makes sense.

In the simulation, all the materials and specifications are precisely the same as in the experimental setup; other input parameters are either directly measured or extrapolated from the measured data in situ. The simulation results are shown in Fig. 16. The temperature sensor near the SiPMs was 6.75 K, as the “T Sensor A (K)” indicates; while the SiPMs’ temperature was 7.1 K. That being said, there was a 0.35 K discrepancy between the temperature sensor and the SiPMs even though they have been mounted on the same copper plate and only have ~ 5 cm distance. According to our experience in simulating other setups, the temperature discrepancy should be ≤ 0.1 K, given the two parts’ configuration. The “abnormal” discrepancy occurred because the SiPMs are connected to a 70 cm SMA cable, through which a preamplifier connected on another end at RT. As a result, the SiPMs has an extra “warm” source from the cable, in addition to the cryogenic source from the integrating sphere. Even by eye, we can see in Fig. 16 that the temperature on the cable’s cold end (near the SiPMs) is higher than the integrating sphere. In the figure, “PD” refers to the photodiode. “T Sensor B” is the temperature sensor near the PD, and “T Sensor C” is the temperature sensor on the cooling plate, which is the cryogenic source of the detector system.

The simulation suggested that the temperature sensor should be 6.75 K. In comparison, the measured one was 10 K, and the ~ 3 K (10 K - 6.75 K) discrepancy is greater than the uncertainty of the temperature sensor, ± 1 K. So, we suspected there should exist other unknown reason(s) being responsible to the temperature discrepancy. We carefully checked the experimental setup and surprisingly spotted a ~ 0.1 mm gap between the copper plate (in which the SiPMs mounted) and the integrating sphere wall, as Fig. 17a shows. We found similar gaps on the other sides of the cubic body. The gaps were due to stress relief during the cooling-down and warming-up cycles. We inserted a 0.5 mm-thick indium film between the plate and the sphere wall, as shown in Fig. 17b. After the upgrade, the temperature sensor near the SiPMs decreased to 7.0 K, 3 K lower than before and consistent with the simulation.

V. CHARACTERIZING THE SIPMS AT 7 K

We re-measured the AP, CT, and PDE at 7 K again the same way as at 10 K. The combined results of AP at 7 K and 10 K are shown in Fig. 18. The plot has the following

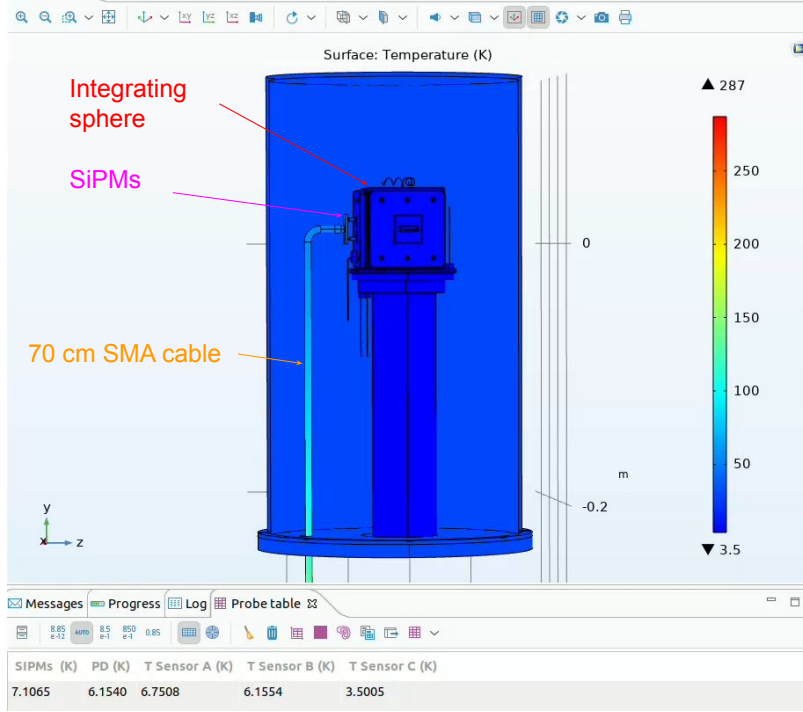


FIG. 16: A COMSOL simulation shows that the SiPMs and the temperature sensor are 7.1065 K and 6.7508 K, respectively. “PD” refers to the photodiode. “T Sensor B” is the temperature sensor near the PD, and “T Sensor B” is the temperature sensor on the cooling plate.

features: (a) the higher the bias voltage, the greater the AP; (b) the AP at 10 K is slightly higher ($\sim 2\%$) than 7 K (for an OV greater than 6 V); (c) for the SiPMs’ possible working bias voltage, OV = 10 V, the measured AP is $\sim 16\%$ at 7 K and 10 K; and (d) with the 6 V OV, the AP we measured are $\sim 9\%$ and 10.5% at 7 K and 10 K, respectively, which are consistent with reference [27]. Although a complete understanding of the AP at cryogenic temperatures is still lacking, reference [27] pointed out two conflicting processes that might help interpret the data. At a lower temperature, the SiPMs’ quenching resistance would increase, which will (i) suppress the avalanche triggering probability in recharge due to a lower voltage applied on the single photon avalanche diode (SPAD) and (ii) have a longer time constant to enhance the chance of a carrier to be released to generate an AP event. However, no known mechanism exists to characterize the AP phenomena precisely at low temperatures. We are communicating with FBK company to better understand our AP results.

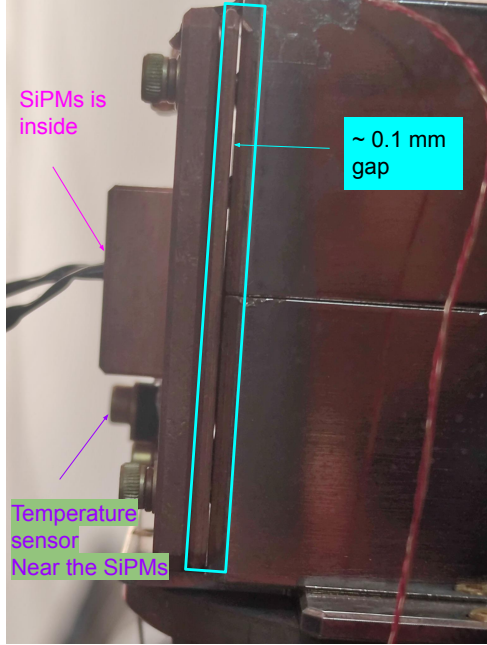


Fig. 17a. A ~ 0.1 mm gap existed between the covering plate and the integrating sphere's wall. The gap made the temperature of the SiPMs and its temperature sensor nearby ~ 3 K higher than it should be.

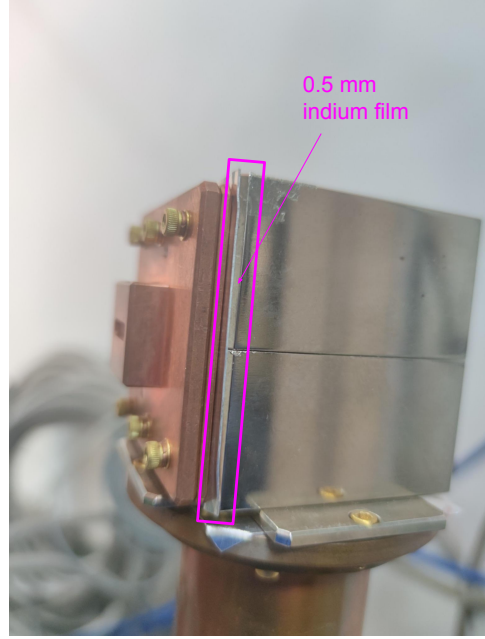


Fig. 17b. The gap was filled with a 0.5 mm-thick indium film. This update led to the measured temperature of the sensor dropping by approximately 3.0 K down to 7.0 K, which aligned well with the simulation in Fig. 16, 6.75 K, confirming the accuracy of our simulation.

FIG. 17: An unexpected ~ 0.1 mm gap led to the temperature of the SiPMs 3 K higher than expected. And a 0.5 mm-thick indium film was inserted to fix the problem.

Regarding the PDE tests, Fig. 19 does not show apparent temperature dependence at 7 K and 10 K. In addition, the plot shows that 405 nm light tends to generate a greater PDE than 530 nm, which is consistent with the tests on the similar type of SiPMs [34] at RT.

The current CT data collected at 7 K was odd. We need more time and data to understand it.

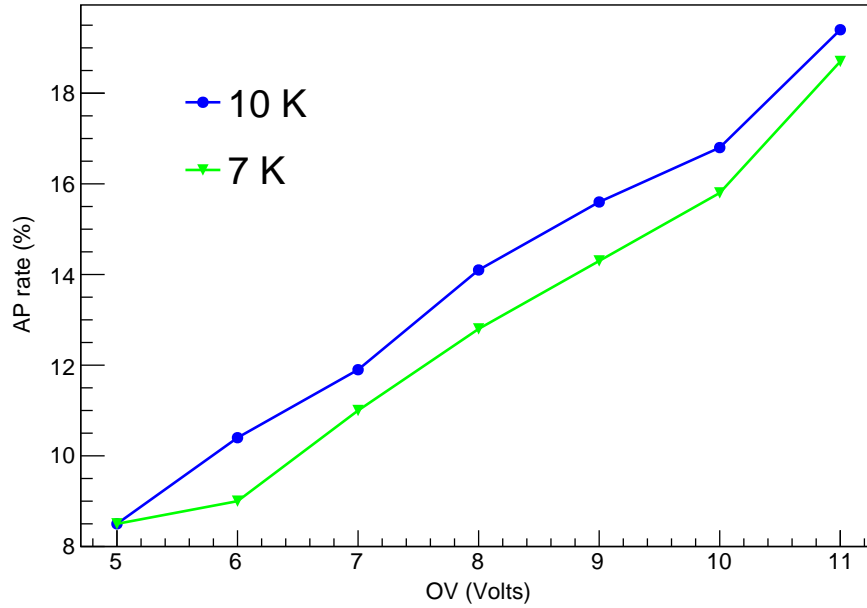


FIG. 18: The combined AP results of an FBK SiPMs worked at 7 K and 10 K when biased with 9 V OV (35 V).

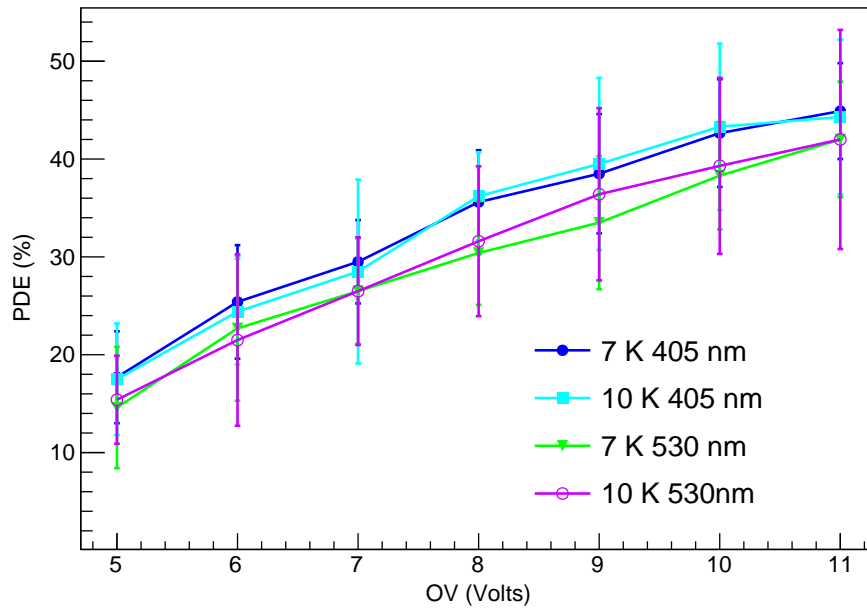


FIG. 19: The combined PDE results of an FBK SiPMs worked at 7 K and 10 K.

VI. DISCUSSION AND SUMMARY

A. Discussion

1. The FBK SiPMs' charge distribution near LHe temperature

As shown in Fig. 7, the typical charge distribution of the FBK NUV-HD-Cryo SiPMs does not show separated Phe peaks at 10 K. We observed similar histograms at room temperature also. However, reference [24, 27, 34] all measured distinct Phe peaks at 77 K or RT on the similar types of FBK SiPMs, as summarized in table II. We do not think our electronics and DAQ should be responsible for the unseparated Phe peaks because (a) as shown in Fig. 6, the noise of the single Phe signal is not significant, and (b) we tested a $4 \times 4 \text{ mm}^2$ Hamamatsu S13370-3050CN SiPMs at RT with almost the same electronics and observed clear peaks. After exchanging a couple of emails with FBK company, we are still far from concluding on this topic. We will continue to discuss this issue with FBK to fully understand it, and we hope to have the desired charge distribution eventually.

TABLE II: Charge testing results of a few types of SiPMs.

Type	Temp	Peaks	Win-size	Cell-pitch	Gain	Reference
	(K)	(Y/N)	(mm^2)	(μm^2)	(E6)	
NUV-HD	300	Y	1×1	25×25	1.5 (OV 5 V)	[34]
NUV-HD	300	Y	1×1	40×40	3.5 (OV 5 V)	[34]
NUV-HD-LF	77	Y	4×4	25×25	0.5 (OV 5 V)	[27]
NUV-HD-LF-HR _q	300	Y	11.7×7.9	25×25	1.4	[24]
NUV-HD-Cryo	7	N	11.7×7.9	30×30	1.3 (OV 11 V)	This work
S13370-3050CN	300	Y	4×4	50×50	2.6 (OV 4 V)	This work

2. Employ the FBK SiPMs into LHe TPCs

Although the lowest temperature the FBK NUV-HD-Cryo SiPMs have been verified to be functional so far is 7 K, instead of the liquid helium temperature of 4.5 K, due to the

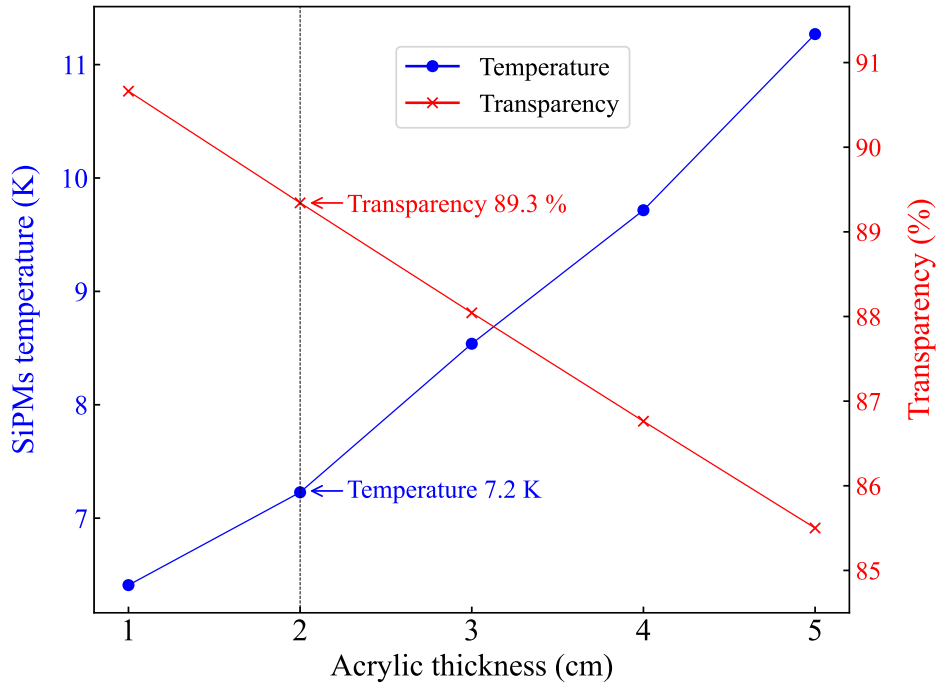


FIG. 20: The COMSOL simulated temperature of the SiPMs and the calculated transparency of the acrylic layer on variant thickness. In the simulation, the liquid side of the acrylic layer was 4.5 K LHe, while the gas side was 1 atm helium gas; the SiPMs were mounted on the acrylic and surrounded by the gas. If the acrylic is 2 cm thick, the acrylic surface’s temperature would be 7.2 K (and the SiPMs’ temperature would be higher), as the left Y-axis shows; while the transparency would be 89.3%, as the right Y-axis. We demonstrated in the manuscript that the FBK NUV-HD-Cryo SiPMs can be functional at 7.0 K.

limitation of the cryocooler, we should be reassured about whether the SiPMs are eligible to work on an LHe TPC or not. The reason is that even if 7 K is the lowest temperature the FBK SiPMs can work, they can still be mounted on the TPC’s top and bottom bases as photosensors provided the SiPMs and the LHe were isolated by a 2-cm thick acrylic. Fig 20 indicates that a 2-cm thick acrylic would keep the SiPMs’ temperature at 7.2 K while maintaining an 89.3% transparency with the same assumption made by DarkSide-20k [24], a 1.5 cm acrylic layer would have a 90% transmission for TPB-converted light.

B. Summary

We have measured the DCR, PDE, AP, and CT on the FBK NUV-HD-Cryo type SiPMs at 7 K and 10 K. The FBK SiPMs showed significantly different performance near LHe temperature than at RT. The DCR is only ~ 0.01 Hz/mm² even with the bias voltage of OV = 12 V, which is equivalent to the Hamamatsu R11410 PMTs installed in the LZ TPC [54]. The PDE reaches the desired 40% when the bias voltage is OV 10 V near LHe temperature. AP and CT are both $\sim 10 - 15$ %, which are reasonably low for the photosensors working for rare events searching experiments. Combing all of the measurements together, we conclude that the FBK NUV-HD-Cryo SiPMs are suitable as photosensors to be equipped on LHe detectors, including but not limited to the ALETHEIA TPCs [9].

ACKNOWLEDGMENTS

We thank the FBK company in Trento, Italy, for sending us the SiPMs. In particular, we thank Dr. Alberto Gola, Dr. Alberto Mazzi, and Dr. Elena Moretti for SiPMs' delivery and other fruitful discussions. We especially thank Dr. Elena Moretti for reading the first version of our manuscript and addressing insightful comments. Dr. Xiangliang Liu and her team at NIM in China have kindly calibrated two photodiodes for us at 6 K on their facilities for free, which we greatly appreciate. In addition, we thank Dr. Wei Hu and Ms. Tangtang Qu at the TOFTEK company for their cooperation in developing readout electronics. We also appreciate Prof. Xiaoguang Wu, Prof. Baozhen Zhao, and Dr. Jinglong Wang at CIAE for their kindness in sharing their devices with us. Junhui Liao would also thank the support of the "Yuanzhang" funding of CIAE to launch the ALETHEIA program. This work has also been supported by NSFC (National Natural Science Foundation of China) under the contract of 12ED232612001001 and the "Continuous-Support Basic Scientific Research Project" in China.

[1] J. Adams, A. Fleischmann, Y. Huang, Y. Kim, R.E.Lanou, H. Maris, and G. Seidel, Progress on heron: A real-time detector for p-p solar neutrinos (2000).

- [2] J. Adouze and J. T. T. Van, eds., *Proceedings of the Dark Matter in XXIII Rencontres de Moriond* (1988).
- [3] *Proceedings of the XXXIst Moriond Conference, Les Arcs, France* (1996).
- [4] W. Guo and D. N. McKinsey, Concept for a dark matter detector using liquid helium-4, *Phys. Rev. D* **87**, 115001 (2013).
- [5] H. J. Maris, G. M. Seidel, and D. Stein, Dark matter detection using helium evaporation and field ionization, *Phys. Rev. Lett.* **119**, 181303 (2017).
- [6] S. A. Hertel, A. Biekert, J. Lin, V. Velan, and D. N. McKinsey, Direct detection of sub-gev dark matter using a superfluid ^4He target, *Phys. Rev. D* **100**, 092007 (2019).
- [7] S. A. Hertel, A. Biekert, J. Lin, V. Velan, and D. N. McKinsey, Direct detection of sub-gev dark matter using a superfluid ^4He target, *Phys. Rev. D* **100**, 092007 (2019).
- [8] A. Biekert, C. Chang, C. W. Fink, M. Garcia-Sciveres, E. C. Glazer, W. Guo, S. A. Hertel, S. Kravitz, J. Lin, M. Lisovenko, R. Mahapatra, D. N. McKinsey, J. S. Nguyen, V. Novosad, W. Page, P. K. Patel, B. Penning, H. D. Pinckney, M. Pyle, R. K. Romani, A. S. Seilnacht, A. Serafin, R. J. Smith, P. Sorensen, B. Suerfu, A. Suzuki, V. Velan, G. Wang, S. L. Watkins, V. G. Yefremenko, L. Yuan, and J. Zhang (SPICE/HeRALD Collaboration), Scintillation yield from electronic and nuclear recoils in superfluid ^4He , *Phys. Rev. D* **105**, 092005 (2022).
- [9] J. Liao, Y. Gao, Z. Liang, Z. Ouyang, Z. Peng, L. Zhang, L. Zhang, J. Zheng, and J. Zhou, Aletheia: hunting for low-mass dark matter with liquid helium tpcs, *The European Physical Journal Plus* **138**, 128 (2023).
- [10] S. Autti, A. Casey, N. Eng, N. Darvishi, P. Franchini, R. P. Haley, P. J. Heikkinen, A. Jennings, A. Kemp, E. Leason, L. V. Levitin, J. Monroe, J. March-Russel, M. T. Noble, J. R. Prance, X. Rojas, T. Salmon, J. Saunders, R. Smith, M. D. Thompson, V. Tsepelin, S. M. West, L. Whitehead, V. V. Zavjalov, and D. E. Zmeev, Quest-dmc superfluid ^3He detector for sub-gev dark matter, *The European Physical Journal C* **84**, 248 (2024).
- [11] P. R. Huffman, C. R. Brome, J. S. Butterworth, K. J. Coakley, M. S. Dewey, S. N. Dzhosyuk, R. Golub, G. L. Greene, K. Habicht, S. K. Lamoreaux, C. E. H. Mattoni, D. N. McKinsey, F. E. Wietfeldt, and J. M. Doyle, Magnetic trapping of neutrons, *Nature* **403**, 62 (2000).
- [12] T. M. Ito, S. M. Clayton, J. Ramsey, M. Karcz, C.-Y. Liu, J. C. Long, T. G. Reddy, and G. M. Seidel, Effect of an electric field on superfluid helium scintillation produced by α -particle sources, *Phys. Rev. A* **85**, 042718 (2012).

- [13] T. M. Ito, J. C. Ramsey, W. Yao, D. H. Beck, V. Cianciolo, S. M. Clayton, C. Crawford, S. A. Currie, B. W. Filippone, W. C. Griffith, M. Makela, R. Schmid, G. M. Seidel, Z. Tang, D. Wagner, W. Wei, and S. E. Williamson, Ito,t. m. and ramsey,j. c. and yao,w. and beck,d. h. and cianciolo,v. and clayton,s. m. and crawford,c. and currie,s. a. and filippone,b. w. and griffith,w. c. and makela,m. and schmid,r. and seidel,g. m. and tang,z. and wagner,d. and wei,w. and williamson,s. e., *Review of Scientific Instruments* **87**, 045113 (2016).
- [14] N. S. Phan, V. Cianciolo, S. M. Clayton, S. A. Currie, R. Dipert, T. M. Ito, S. W. T. MacDonald, C. M. O'Shaughnessy, J. C. Ramsey, G. M. Seidel, E. Smith, E. Tang, Z. Tang, and W. Yao, Effect of an electric field on liquid helium scintillation produced by fast electrons, *Phys. Rev. C* **102**, 035503 (2020).
- [15] S. Kubota, T. Takahashi, and T. Doke, Mechanism of scintillation of helium, helium-argon, and helium-neon gas mixtures excited by alpha particles, *Phys. Rev.* **165** (1968).
- [16] C. Benson, G. D. Orebi Gann, and V. Gehman, Measurements of the intrinsic quantum efficiency and absorption length of tetraphenyl butadiene thin films in the vacuum ultraviolet regime, *The European Physical Journal C* **78**, 10.1140/epjc/s10052-018-5807-z (2018).
- [17] For superfluid liquid helium detectors, the required temperature for a photosensor would be even lower than 4.5 K, and the exact temperature depends on the detector system.
- [18] *2014 IEEE Nuclear Science Symposium and Medical Imaging Conference (NSS/MIC)* (2014).
- [19] R. Iwai, M. Sakurai, A. Antognini, I. Belosevic, M. Hildebrandt, K. Kirch, A. Knecht, A. Papa, and A. Stoykov, Characterization of cryogenic sipm down to 6.5k, *JPS Conference Proceedings* (2019), <https://journals.jps.jp/doi/pdf/10.7566/JPSCP.27.012005>.
- [20] J. Zhang, D. Goeldi, R. Iwai, M. Sakurai, and A. Soter, Scintillation detectors with silicon photomultiplier readout in a dilution refrigerator at temperatures down to 0.2 k, *Journal of Instrumentation* **17** (06), P06024.
- [21] J. Aalbers, D. S. Akerib, C. W. Akerlof, A. K. Al Musalhi, F. Alder, A. Alqahtani, S. K. Alsum, C. S. Amarasinghe, A. Ames, T. J. Anderson, N. Angelides, H. M. Araújo, J. E. Armstrong, M. Arthurs, S. Azadi, A. J. Bailey, A. Baker, J. Balajthy, S. Balashov, J. Bang, J. W. Bargemann, M. J. Barry, J. Barthel, D. Bauer, A. Baxter, K. Beattie, J. Belle, P. Beltrame, J. Bensinger, T. Benson, E. P. Bernard, A. Bhatti, A. Biekert, T. P. Biesiadzinski, H. J. Birch, B. Birrittella, G. M. Blockinger, K. E. Boast, B. Boxer, R. Bramante, C. A. J. Brew, P. Brás, J. H. Buckley, V. V. Bugaev, S. Burdin, J. K. Busenitz, M. Buuck, R. Cabrera, C. Carels, D. L.

Carlsmith, B. Carlson, M. C. Carmona-Benitez, M. Cascella, C. Chan, A. Chawla, H. Chen, J. J. Cherwinka, N. I. Chott, A. Cole, J. Coleman, M. V. Converse, A. Cottle, G. Cox, W. W. Craddock, O. Creaner, D. Curran, A. Currie, J. E. Cutter, C. E. Dahl, A. David, J. Davis, T. J. R. Davison, J. Delgaudio, S. Dey, L. de Viveiros, A. Dobi, J. E. Y. Dobson, E. Druszkiewicz, A. Dushkin, T. K. Edberg, W. R. Edwards, M. M. Elnimr, W. T. Emmet, S. R. Eriksen, C. H. Faham, A. Fan, S. Fayer, N. M. Fearon, S. Fiorucci, H. Flaecher, P. Ford, V. B. Francis, E. D. Fraser, T. Fruth, R. J. Gaitskell, N. J. Gantos, D. Garcia, A. Geffre, V. M. Gehman, J. Genovesi, C. Ghag, R. Gibbons, E. Gibson, M. G. D. Gilchriese, S. Gokhale, B. Gomber, J. Green, A. Greenall, S. Greenwood, M. G. D. van der Grinten, C. B. Gwilliam, C. R. Hall, S. Hans, K. Hanzel, A. Harrison, E. Hartigan-O'Connor, S. J. Haselschwardt, M. A. Hernandez, S. A. Hertel, G. Heuermann, C. Hjermfelt, M. D. Hoff, E. Holtom, J. Y.-K. Hor, M. Horn, D. Q. Huang, D. Hunt, C. M. Ignarra, R. G. Jacobsen, O. Jahangir, R. S. James, S. N. Jeffery, W. Ji, J. Johnson, A. C. Kaboth, A. C. Kamaha, K. Kamdin, V. Kasey, K. Kazkaz, J. Keefner, D. Khaitan, M. Khaleeq, A. Khazov, I. Khurana, Y. D. Kim, C. D. Kocher, D. Kodroff, L. Korley, E. V. Korolkova, J. Kras, H. Kraus, S. Kravitz, H. J. Krebs, L. Kreczko, B. Krikler, V. A. Kudryavtsev, S. Kyre, B. Landerud, E. A. Leason, C. Lee, J. Lee, D. S. Leonard, R. Leonard, K. T. Lesko, C. Levy, J. Li, F.-T. Liao, J. Liao, J. Lin, A. Lindote, R. Linehan, W. H. Lippincott, R. Liu, X. Liu, Y. Liu, C. Loniewski, M. I. Lopes, E. Lopez Asamar, B. López Paredes, W. Lorenzon, D. Lucero, S. Luitz, J. M. Lyle, P. A. Majewski, J. Makkinje, D. C. Malling, A. Manalaysay, L. Manenti, R. L. Mannino, N. Marangou, M. F. Marzioni, C. Maupin, M. E. McCarthy, C. T. McConnell, D. N. McKinsey, J. McLaughlin, Y. Meng, J. Migneault, E. H. Miller, E. Mizrachi, J. A. Mock, A. Monte, M. E. Monzani, J. A. Morad, J. D. Morales Mendoza, E. Morrison, B. J. Mount, M. Murdy, A. S. J. Murphy, D. Naim, A. Naylor, C. Nedlik, C. Nehr Korn, F. Neves, A. Nguyen, J. A. Nikoleyczik, A. Nilima, J. O'Dell, F. G. O'Neill, K. O'Sullivan, I. Olcina, M. A. Olevitch, K. C. Oliver-Mallory, J. Orpwood, D. Pagenkopf, S. Pal, K. J. Palladino, J. Palmer, M. Pangilinan, N. Parveen, S. J. Patton, E. K. Pease, B. Penning, C. Pereira, G. Pereira, E. Perry, T. Pershing, I. B. Peterson, A. Piepke, J. Podczerwinski, D. Porzio, S. Powell, R. M. Preece, K. Pushkin, Y. Qie, B. N. Ratcliff, J. Reichenbacher, L. Reichhart, C. A. Rhyne, A. Richards, Q. Riffard, G. R. C. Rischbieter, J. P. Rodrigues, A. Rodriguez, H. J. Rose, R. Rosero, P. Rossiter, T. Rushton, G. Rutherford, D. Rynders, J. S. Saba, D. Santone, A. B. M. R. Sazzad, R. W.

Schnee, P. R. Scovell, D. Seymour, S. Shaw, T. Shutt, J. J. Silk, C. Silva, G. Sinev, K. Skarpaas, W. Skulski, R. Smith, M. Solmaz, V. N. Solovov, P. Sorensen, J. Soria, I. Stancu, M. R. Stark, A. Stevens, T. M. Stiegler, K. Stifter, R. Studley, B. Suerfu, T. J. Sumner, P. Sutcliffe, N. Swanson, M. Szydagis, M. Tan, D. J. Taylor, R. Taylor, W. C. Taylor, D. J. Temples, B. P. Tennyson, P. A. Terman, K. J. Thomas, D. R. Tiedt, M. Timalina, W. H. To, A. Tomás, Z. Tong, D. R. Tovey, J. Tranter, M. Trask, M. Tripathi, D. R. Tronstad, C. E. Tull, W. Turner, L. Tvrznikova, U. Utku, J. Va'vra, A. Vacheret, A. C. Vaitkus, J. R. Verbus, E. Voirin, W. L. Waldron, A. Wang, B. Wang, J. J. Wang, W. Wang, Y. Wang, J. R. Watson, R. C. Webb, A. White, D. T. White, J. T. White, R. G. White, T. J. Whitis, M. Williams, W. J. Wisniewski, M. S. Witherell, F. L. H. Wolfs, J. D. Wolfs, S. Woodford, D. Woodward, S. D. Worm, C. J. Wright, Q. Xia, X. Xiang, Q. Xiao, J. Xu, M. Yeh, J. Yin, I. Young, P. Zarzhitsky, A. Zuckerman, and E. A. Zweig (LUX-ZEPLIN Collaboration), First dark matter search results from the lux-zeplin (lz) experiment (2023).

- [22] E. Aprile, K. Abe, F. Agostini, S. Ahmed Maouloud, L. Althueser, B. Andrieu, E. Angelino, J. R. Angevaere, V. C. Antochi, D. Antón Martín, F. Arneodo, L. Baudis, A. L. Baxter, M. Bazyk, L. Bellagamba, R. Biondi, A. Bismark, E. J. Brookes, A. Brown, S. Bruenner, G. Bruno, R. Budnik, T. K. Bui, C. Cai, J. M. R. Cardoso, D. Cichon, A. P. Cimental Chavez, A. P. Colijn, J. Conrad, J. J. Cuenca-García, J. P. Cussonneau, V. D'Andrea, M. P. Decowski, P. Di Gangi, S. Di Pede, S. Diglio, K. Eitel, A. Elykov, S. Farrell, A. D. Ferella, C. Ferrari, H. Fischer, M. Flierman, W. Fulgione, C. Fuselli, P. Gaemers, R. Gaior, A. Gallo Rosso, M. Galloway, F. Gao, R. Glade-Beucke, L. Grandi, J. Grigat, H. Guan, M. Guida, R. Hammann, A. Higuera, C. Hils, L. Hoetzsch, N. F. Hood, J. Howlett, M. Iacovacci, Y. Itow, J. Jakob, F. Joerg, A. Joy, N. Kato, M. Kara, P. Kavargin, S. Kazama, M. Kobayashi, G. Koltman, A. Kopec, F. Kuger, H. Landsman, R. F. Lang, L. Levinson, I. Li, S. Li, S. Liang, S. Lindemann, M. Lindner, K. Liu, J. Loizeau, F. Lombardi, J. Long, J. A. M. Lopes, Y. Ma, C. Macolino, J. Mahlstedt, A. Mancuso, L. Manenti, F. Marignetti, T. Marrodán Undagoitia, K. Martens, J. Masbou, D. Masson, E. Masson, S. Mastroianni, M. Messina, K. Miuchi, K. Mizukoshi, A. Molinario, S. Moriyama, K. Morã, Y. Mosbacher, M. Murra, J. Müller, K. Ni, U. Oberlack, B. Paetsch, J. Palacio, R. Peres, C. Peters, J. Pienaar, M. Pierre, V. Pizzella, G. Plante, J. Qi, J. Qin, D. Ramírez García, R. Singh, L. Sanchez, J. M. F. dos Santos, I. Sarnoff, G. Sartorelli, J. Schreiner, D. Schulte, P. Schulte, H. Schulze Eißing, M. Schumann,

- L. Scotto Lavina, M. Selvi, F. Semeria, P. Shagin, S. Shi, E. Shockley, M. Silva, H. Simgen, A. Takeda, P.-L. Tan, A. Terliuk, D. Thers, F. Toschi, G. Trincherro, C. Tunnell, F. Tönnies, K. Valerius, G. Volta, C. Weinheimer, M. Weiss, D. Wenz, C. Wittweg, T. Wolf, V. H. S. Wu, Y. Xing, D. Xu, Z. Xu, M. Yamashita, L. Yang, J. Ye, L. Yuan, G. Zavattini, M. Zhong, and T. Zhu (XENON Collaboration), First dark matter search with nuclear recoils from the xenonnt experiment, *Phys. Rev. Lett.* **131**, 041003 (2023).
- [23] Y. Meng, Z. Wang, Y. Tao, A. Abdukerim, Z. Bo, W. Chen, X. Chen, Y. Chen, C. Cheng, Y. Cheng, X. Cui, Y. Fan, D. Fang, C. Fu, M. Fu, L. Geng, K. Giboni, L. Gu, X. Guo, K. Han, C. He, J. He, D. Huang, Y. Huang, Z. Huang, R. Hou, X. Ji, Y. Ju, C. Li, M. Li, S. Li, S. Li, Q. Lin, J. Liu, X. Lu, L. Luo, W. Ma, Y. Ma, Y. Mao, N. Shaheed, X. Ning, N. Qi, Z. Qian, X. Ren, C. Shang, G. Shen, L. Si, W. Sun, A. Tan, A. Wang, M. Wang, Q. Wang, S. Wang, S. Wang, W. Wang, X. Wang, M. Wu, W. Wu, J. Xia, M. Xiao, X. Xiao, P. Xie, B. Yan, X. Yan, J. Yang, Y. Yang, C. Yu, J. Yuan, Y. Yuan, D. Zhang, M. Zhang, P. Zhang, T. Zhang, L. Zhao, Q. Zheng, J. Zhou, N. Zhou, X. Zhou, and Y. Zhou (PandaX-4T Collaboration), Dark matter search results from the pandax-4t commissioning run, *Phys. Rev. Lett.* **127**, 261802 (2021).
- [24] C. E. Aalseth, F. Acerbi, P. Agnes, I. F. M. Albuquerque, T. Alexander, A. Alici, A. K. Alton, P. Antonioli, S. Arcelli, R. Ardito, and et al., Darkside-20k: A 20 tonne two-phase lar tpc for direct dark matter detection at lngs, *The European Physical Journal Plus* **133**, 10.1140/epjp/i2018-11973-4 (2018).
- [25] R. Ajaj, P.-A. Amaudruz, G. R. Araujo, M. Baldwin, M. Batygov, B. Beltran, C. E. Bina, J. Bonatt, M. G. Boulay, B. Broerman, J. F. Bueno, P. M. Burghardt, A. Butcher, B. Cai, S. Cavuoti, M. Chen, Y. Chen, B. T. Cleveland, D. Cranshaw, K. Dering, J. DiGiuseffo, L. Doria, F. A. Duncan, M. Dunford, A. Erlandson, N. Fatemighomi, G. Fiorillo, S. Florian, A. Flower, R. J. Ford, R. Gagnon, D. Gallacher, E. A. Garcés, S. Garg, P. Giampa, D. Goeldi, V. V. Golovko, P. Gorel, K. Graham, D. R. Grant, A. L. Hallin, M. Hamstra, P. J. Harvey, C. Hearns, A. Joy, C. J. Jillings, O. Kamaev, G. Kaur, A. Kemp, I. Kochanek, M. Kuźniak, S. Langrock, F. La Zia, B. Lehnert, X. Li, J. Lidgard, T. Lindner, O. Litvinov, J. Lock, G. Longo, P. Majewski, A. B. McDonald, T. McElroy, T. McGinn, J. B. McLaughlin, R. Mehdiyev, C. Mielnichuk, J. Monroe, P. Nadeau, C. Nantais, C. Ng, A. J. Noble, E. O’Dwyer, C. Ouellet, P. Pasuthip, S. J. M. Peeters, M.-C. Piro, T. R. Pollmann, E. T. Rand,

- C. Rethmeier, F. Retière, N. Seeburn, K. Singhrao, P. Skensved, B. Smith, N. J. T. Smith, T. Sonley, J. Soukup, R. Stainforth, C. Stone, V. Strickland, B. Sur, J. Tang, E. Vázquez-Jáuregui, L. Veloce, S. Viel, J. Walding, M. Waqar, M. Ward, S. Westerdale, J. Willis, and A. Zuñiga Reyes, Search for dark matter with a 231-day exposure of liquid argon using deep-3600 at snolab, *Phys. Rev. D* **100**, 022004 (2019).
- [26] H. company, *Photomultiplier tubes, basics and applications*, Hamamatsu company, fourth edition ed. (2017).
- [27] F. Acerbi, S. Davini, A. Ferri, C. Galbiati, G. Giovanetti, A. Gola, G. Korga, A. Mandarano, M. Marcante, G. Paternoster, C. Piemonte, A. Razeto, V. Regazzoni, D. Sablone, C. Savarese, G. Zappalá, and N. Zorzi, Cryogenic characterization of fbk hd near-uv sensitive sipms, *IEEE Transactions on Electron Devices* **64**, 521 (2017).
- [28] A. Phipps, A. Juillard, B. Sadoulet, B. Serfass, and Y. Jin, A hemt-based cryogenic charge amplifier with sub-100 evec ionization resolution for massive semiconductor dark matter detectors, *Nuclear Instruments and Methods in Physics Research Section A: Accelerators, Spectrometers, Detectors and Associated Equipment* **940**, 181 (2019).
- [29] J. Anczarski, M. Dubovskov, C. W. Fink, S. Kevane, N. A. Kurinsky, S. J. Meijer, A. Phipps, F. Ronning, I. Rydstrom, A. Simchony, Z. Smith, S. M. Thomas, S. L. Watkins, and B. A. Young, Two-stage cryogenic hemt based amplifier for low temperature detectors (2023), arXiv:2311.02229.
- [30] A. Cardini, D. Brundu, V. Fanti, A. Lai, and A. Loi, Operation of silicon photomultipliers at liquid helium temperature, in *2014 IEEE Nuclear Science Symposium and Medical Imaging Conference (NSS/MIC)* (2014) pp. 1–6.
- [31] <https://www.thinksrs.com/products/dg535.html>.
- [32] <https://optodiode.com>.
- [33] P. Eckert, H.-C. Schultz-Coulon, W. Shen, R. Stamen, and A. Tadday, Characterisation studies of silicon photomultipliers, *Nuclear Instruments and Methods in Physics Research Section A: Accelerators, Spectrometers, Detectors and Associated Equipment* **620**, 217 (2010).
- [34] G. Zappala, F. Acerbi, A. Ferri, A. Gola, G. Paternoster, N. Zorzi, and C. Piemonte, Set-up and methods for sipm photo-detection efficiency measurements, *Journal of Instrumentation* **11** (08), P08014.
- [35] H. company, *MPPC Technical Note*, Hamamatsu company (2021).

- [36] J. H. at NIST, private communication with nist on calibrating the responsivity of a photodiode at the temperature (2023).
- [37] private communication with dr. alberto gola and other fbk people (2019 - 2023).
- [38] Assuming the SiPMs' gain is 10^6 at 10 K with a bias higher than the breakdown voltage. Given the DCR is 1 Hz, the current would only be $0.16 \text{ pA} = 1.6 \cdot 10^{-19} \text{ C} \times 1 \text{ Hz} \times 10^6$, where $1.6 \cdot 10^{-19} \text{ C}$ is the charge of an electron. At room temperature however, the DCR often is 10^7 Hz scale and the gain is 10^6 , the current would be $1.6 \text{ } \mu\text{A} = 1.6 \cdot 10^{-19} \text{ C} \times 10^7 \text{ Hz} \times 10^6$.
- [39] C. R. Crowell and S. M. Sze, TEMPERATURE DEPENDENCE OF AVALANCHE MULTIPLICATION IN SEMICONDUCTORS, *Applied Physics Letters* **9**, 242 (1968), https://pubs.aip.org/aip/apl/article-pdf/9/6/242/18419234/242_1_online.pdf.
- [40] A. Otte, J. Hose, R. Mirzoyan, A. Romaszkiwicz, M. Teshima, and A. Thea, A measurement of the photon detection efficiency of silicon photomultipliers, *Nuclear Instruments and Methods in Physics Research Section A: Accelerators, Spectrometers, Detectors and Associated Equipment* **567**, 360 (2006), proceedings of the 4th International Conference on New Developments in Photodetection.
- [41] P. Finocchiaro, A. Pappalardo, L. Cosentino, M. Belluso, S. Billotta, G. Bonanno, and S. Di Mauro, Features of silicon photo multipliers: Precision measurements of noise, cross-talk, afterpulsing, detection efficiency, *IEEE Transactions on Nuclear Science* **56**, 1033 (2009).
- [42] S. K. Yang, J. Lee, S.-W. Kim, H.-Y. Lee, J.-A. Jeon, I. H. Park, J.-R. Yoon, and Y.-S. Baek, Precision measurement of the photon detection efficiency of silicon photomultipliers using two integrating spheres, *Opt. Express* **22**, 716 (2014).
- [43] C. Piemonte, F. Acerbi, A. Ferri, A. Gola, G. Paternoster, V. Regazzoni, G. Zappala, and N. Zorzi, Performance of nuv-hd silicon photomultiplier technology, *IEEE Transactions on Electron Devices* **63**, 1111 (2016).
- [44] C. Piemonte, A. Ferri, A. Gola, A. Picciotto, T. Pro, N. Serra, A. Tarolli, and N. Zorzi, Development of an automatic procedure for the characterization of silicon photomultipliers, in *2012 IEEE Nuclear Science Symposium and Medical Imaging Conference Record (NSS/MIC)* (2012) pp. 428–432.
- [45] CERN, Root website.

- [46] L. Bonnet, J. Liao, and K. Piotrkowski, Study on gastof – a 10ps resolution timing detector, Nuclear Instruments and Methods in Physics Research Section A: Accelerators, Spectrometers, Detectors and Associated Equipment **762**, 77 (2014).
- [47] L. Baudis, A. Behrens, A. Ferella, A. Kish, T. M. Undagoitia, D. Mayani, and M. Schumann, Performance of the hamamatsu r11410 photomultiplier tube in cryogenic xenon environments, JINST **9** (P04026).
- [48] D. Akerib, C. Akerlof, A. Alqahtani, S. Alsum, T. Anderson, N. Angelides, H. Araújo, J. Armstrong, M. Arthurs, X. Bai, J. Balajthy, S. Balashov, J. Bang, D. Bauer, A. Baxter, J. Bensinger, E. Bernard, A. Bernstein, A. Bhatti, A. Biekert, T. Biesiadzinski, H. Birch, K. Boast, B. Boxer, P. Brás, J. Buckley, V. Bugaev, S. Burdin, J. Busenitz, R. Cabrita, C. Carels, D. Carlsmith, M. Carmona-Benitez, M. Cascella, C. Chan, N. Chott, A. Cole, A. Cottle, J. Cutter, C. Dahl, L. de Viveiros, J. Dobson, E. Druszkiewicz, T. Edberg, S. Erikson, A. Fan, S. Fayer, S. Fiorucci, H. Flaecher, E. Fraser, T. Fruth, R. Gaitskell, J. Genovesi, C. Ghag, E. Gibson, M. Gilchriese, S. Gokhale, M. van der Grinten, C. Hall, A. Harrison, S. Haselschwardt, S. Hertel, J.-K. Hor, M. Horn, D. Huang, C. Ignarra, O. Jahangir, W. Ji, J. Johnson, A. Kaboth, A. Kamaha, K. Kamdin, K. Kazkaz, D. Khaitan, A. Khazov, I. Khurana, C. Kocher, L. Korley, E. Korolkova, J. Kras, H. Kraus, S. Kravitz, L. Kreczko, B. Krikler, V. Kudryavtsev, E. Leason, J. Lee, D. Leonard, K. Lesko, C. Levy, J. Li, J. Liao, F.-T. Liao, J. Lin, A. Lindote, R. Linehan, W. Lippincott, R. Liu, X. Liu, C. Loniewski, M. Lopes, B. López Paredes, W. Lorenzon, S. Luitz, J. Lyle, P. Majewski, A. Manalaysay, L. Manenti, R. Mannino, N. Marangou, M. Marzioni, D. McKinsey, J. McLaughlin, Y. Meng, E. Miller, E. Mizrachi, A. Monte, M. Monzani, J. Morad, E. Morrison, B. Mount, A. Murphy, D. Naim, A. Naylor, C. Nedlik, C. Nehr Korn, H. Nelson, F. Neves, J. Nikoleyczik, A. Nilima, I. Olcina, K. Oliver-Mallory, S. Pal, K. Palladino, J. Palmer, N. Parveen, E. Pease, B. Penning, G. Pereira, A. Piepke, K. Pushkin, J. Reichenbacher, C. Rhyne, A. Richards, Q. Riffard, G. Rischbieter, R. Rosero, P. Rossiter, G. Rutherford, D. Santone, A. Sazzad, R. Schnee, M. Schubnell, P. Scovell, D. Seymour, S. Shaw, T. Shutt, J. Silk, C. Silva, R. Smith, M. Solmaz, V. Solovov, P. Sorensen, I. Stancu, A. Stevens, K. Stifter, T. Sumner, N. Swanson, M. Szydagis, M. Tan, W. Taylor, R. Taylor, D. Temples, P. Terman, D. Tiedt, M. Timalisina, A. Tomás, M. Tripathi, D. Tronstad, W. Turner, L. Tvrznikova, U. Utku, A. Vacheret, A. Vaitkus, J. Wang, W. Wang, J. Watson, R. Webb, R. White, T. Whitis, F. Wolfs, D. Woodward,

- X. Xiang, J. Xu, M. Yeh, and P. Zarzhitsky, Simulations of events for the lux-zeplin (lz) dark matter experiment, *Astroparticle Physics* **125**, 102480 (2021).
- [49] G. Collazuol, M. Bisogni, S. Marcatili, C. Piemonte, and A. Del Guerra, Studies of silicon photomultipliers at cryogenic temperatures, *Nuclear Instruments and Methods in Physics Research Section A: Accelerators, Spectrometers, Detectors and Associated Equipment* **628**, 389 (2011).
- [50] R. Álvarez-Garrote, E. Calvo, A. Canto, J. Crespo-Anadón, C. Cuesta, A. de la Torre Rojo, I. Gil-Botella, S. Manthey Corchado, I. Martín, C. Palomares, L. Pérez-Molina, and A. Verdugo de Osa, Measurement of the photon detection efficiency of hamamatsu vuv4 sipms at cryogenic temperature, *Nuclear Instruments and Methods in Physics Research Section A: Accelerators, Spectrometers, Detectors and Associated Equipment* **1064**, 169347 (2024).
- [51] The 40 mV was measured with a $5\times$ amplifier connected upstream. So, it is equivalent to 8 mV in Fig. 6, which was directly measured on the preamplifier's output.
- [52] S. Vinogradov, Analytical models of probability distribution and excess noise factor of solid state photomultiplier signals with crosstalk, *Nucl. Instrum. Methods (A)* **695**, 247 (2012).
- [53] Comsol official website (2023).
- [54] B. J. Mount, S. Hans, R. Rosero, M. Yeh, C. Chan, R. J. Gaitskell, D. Q. Huang, J. Makkinje, D. C. Malling, M. Pangilinan, C. A. Rhyne, W. C. Taylor, J. R. Verbus, Y. D. Kim, H. S. Lee, J. Lee, D. S. Leonard, J. Li, J. Belle, A. Cottle, W. H. Lippincott, D. J. Markley, T. J. Martin, M. Sarychev, T. E. Tope, M. Utes, R. Wang, I. Young, H. M. Araújo, A. J. Bailey, D. Bauer, D. Colling, A. Currie, S. Fayer, F. Froberg, S. Greenwood, W. G. Jones, V. Kasey, M. Khaleeq, I. Olcina, B. L. Paredes, A. Richards, T. J. Sumner, A. Tomás, A. Vacheret, P. Brás, A. Lindote, M. I. Lopes, F. Neves, J. P. Rodrigues, C. Silva, V. N. Solovov, M. J. Barry, A. Cole, A. Dobi, W. R. Edwards, C. H. Faham, S. Fiorucci, N. J. Gantos, V. M. Gehman, M. G. D. Gilchriese, K. Hanzel, M. D. Hoff, K. Kamdin, K. T. Lesko, C. T. McConnell, K. O'Sullivan, K. C. Oliver-Mallory, S. J. Patton, J. S. Saba, P. Sorensen, K. J. Thomas, C. E. Tull, W. L. Waldron, M. S. Witherell, A. Bernstein, K. Kazkaz, J. Xu, D. Y. Akimov, A. I. Bolozdynya, A. V. Khromov, A. M. Konovalov, A. V. Kumpan, V. V. Sosnovtsev, C. E. Dahl, D. Temples, M. C. Carmona-Benitez, L. de Viveiros, D. S. Akerib, H. Auyeung, T. P. Biesiadzinski, M. Breidenbach, R. Bramante, R. Conley, W. W. Craddock, A. Fan, A. Hau, C. M. Ignarra, W. Ji, H. J. Krebs, R. Linehan, C. Lee, S. Luitz, E. Mizrachi,

M. E. Monzani, F. G. O'Neill, S. Pierson, M. Racine, B. N. Ratcliff, G. W. Shutt, T. A. Shutt, K. Skarpaas, K. Stifter, W. H. To, J. Va'vra, T. J. Whitis, W. J. Wisniewski, X. Bai, R. Bunker, R. Coughlen, C. Hjermfelt, R. Leonard, E. H. Miller, E. Morrison, J. Reichenbacher, R. W. Schnee, M. R. Stark, K. Sundarnath, D. R. Tiedt, M. Timalsina, P. Bauer, B. Carlson, M. Horn, M. Johnson, J. Keefner, C. Maupin, D. J. Taylor, S. Balashov, P. Ford, V. Francis, E. Holtom, A. Khazov, A. Kaboth, P. Majewski, J. A. Nikkel, J. O'Dell, R. M. Preece, M. G. D. van der Grinten, S. D. Worm, R. L. Mannino, T. M. Stiegler, P. A. Terman, R. C. Webb, C. Levy, J. Mock, M. Szydagis, J. K. Busenitz, M. Elnimr, J. Y.-K. Hor, Y. Meng, A. Piepke, I. Stancu, L. Kreczko, B. Krikler, B. Penning, E. P. Bernard, R. G. Jacobsen, D. N. McKinsey, R. Watson, J. E. Cutter, S. El-Jurf, R. M. Gerhard, D. Hemer, S. Hillbrand, B. Holbrook, B. G. Lenardo, A. G. Manalaysay, J. A. Morad, S. Stephenson, J. A. Thomson, M. Tripathi, S. Uvarov, S. J. Haselschwardt, S. Kyre, C. Nehr Korn, H. N. Nelson, M. Solmaz, D. T. White, M. Cascella, J. E. Y. Dobson, C. Ghag, X. Liu, L. Manenti, L. Reichhart, S. Shaw, U. Utku, P. Beltrame, T. J. R. Davison, M. F. Marzioni, A. S. J. Murphy, A. Nilima, B. Boxer, S. Burdin, A. Greenall, S. Powell, H. J. Rose, P. Sutcliffe, J. Balajthy, T. K. Edberg, C. R. Hall, J. S. Silk, S. Hertel, C. W. Akerlof, M. Arthurs, W. Lorenzon, K. Pushkin, M. Schubnell, K. E. Boast, C. Carels, T. Fruth, H. Kraus, F. T. Liao, J. Lin, P. R. Scovell, E. Druszkiewicz, D. Khaitan, M. Koyuncu, W. Skulski, F. L. H. Wolfs, J. Yin, E. V. Korolkova, V. A. Kudryavtsev, P. Rossiter, D. Woodward, A. A. Chiller, C. Chiller, D. M. Mei, L. Wang, W. Z. Wei, M. While, C. Zhang, S. K. Alsum, T. Benson, D. L. Carlsmith, J. J. Cherwinka, S. Dasu, G. Gregerson, B. Gomber, A. Pagac, K. J. Palladino, C. O. Vuosalo, Q. Xiao, J. H. Buckley, V. V. Bugaev, M. A. Olevitch, E. M. Boulton, W. T. Emmet, T. W. Hurteau, N. A. Larsen, E. K. Pease, B. P. Tennyson, and L. Tvrznikova, Lux-zeplin (lz) technical design report (2017), arXiv:1703.09144 [physics.ins-det].